Controls on the Thermomechanical Evolution of Hyperextended Lithosphere at Magma-Poor Rifted Margins: The Example of Espirito Santo and the Kwanza Basins

L.L. Lavier, P. Ball, G. Manatschal, M. Heumann, J. Macdonald, V. Matt, C. Schneider

Geochemistry, Geophysics, Geosystems

RESEARCH ARTICLE
10.1029/2019GC008580

Special Section:
Wilson Cycles and the Formation of Marginal Basins: Rifting Dynamics and Mantle Evolution from Mid-ocean Ridge Creation to Extinction

Controls on the Thermomechanical Evolution of Hyperextended Lithosphere at Magma-Poor Rifted Margins: The Example of Espirito Santo and the Kwanza Basins

L.L. Lavier[1,2], P. J. Ball[3], G. Manatschal[4], M. J. Heumann[5], J. MacDonald[6], V. J. Matt[7], and C. Schneider[7]

[1]Department of Geological Sciences, University of Texas at Austin, Austin, TX, USA, [2]Institute for Geophysics, University of Texas at Austin, Austin, TX, USA, [3]School of Geography, Geology and the Environment, Keele University, Newcastle, UK, [4]IPGS-EOST, Université de Strasbourg-CNRS, Strasbourg, France, [5]Apache Corporation, Houston, TX, USA, [6]ConocoPhillips, Anchorage, AK, USA, [7]ConocoPhillips, Houston, TX, USA

Key Points:
- Models of rift to seafloor spreading are consistent with first-order observations of tectonic/thermal evolution of hyper-extended margins
- We propose a new rheological formulation for the formation of shear zone in the semibrittle crust and mantle
- Model also highlights the progressive evolution and formation of low-angle shear zones as rifting evolves

Supporting Information:
- Supporting Information S1
- Table S1
- Movie S1

Correspondence to:
L. L. Lavier,
luc@jsg.utexas.edu

Citation:
Lavier, L. L., Ball, P. J., Manatschal, G., Heumann, M. J., MacDonald, J., Matt, V. J., & Schneider, C. (2019). Controls on the thermomechanical evolution of hyperextended lithosphere at magma-poor rifted margins: The example of Espirito Santo and the Kwanza basins. *Geochemistry, Geophysics, Geosystems*, *20*, 5148–5176. https://doi.org/10.1029/2019GC008580

Received 22 JUL 2019
Accepted 11 SEP 2019
Accepted article online 31 OCT 2019
Published online 19 NOV 2019

Abstract High-quality, long offset seismic data from many distal rifted margins show evidence for hyper-extended, <10-km-thick crust. Direct observation of such domains is challenging as they lie, at great water depth, buried beneath thick sedimentary sequences and formed by rock-assemblages that are hydrated and geophysically indistinguishable. Only a few drill holes have penetrated basement at ultradistal rifted margins. These observations, together with outcrops of preserved analogs exposed in collisional orogens, suggest that the complex interaction of detachment faults rooted in a subhorizontal shear zone in the hyperextended crust or, in the serpentinized mantle controls the formation of the ocean continent transition. While depth-dependent thinning controls the early phases of rifting conforming to classical rift models, we still have a superficial understanding of how normal faults and subhorizontal shear zones form and evolve during rifting and lithospheric breakup. Here we develop a rheological parameterization to simulate the formation of, and slip-on, large offset normal faults rooted in growing brittle to ductile shear zones. The evolution of these structures leads to the creation of a hyperextended crust and eventually exhumed serpentinized mantle. We also propose a simplified formulation to simulate magmatic underplating and seafloor spreading. The resulting numerical models provide a self-consistent picture for the evolution of magma-poor rifted margins from initiation of rifting to seafloor spreading. The model results are compared with first-order observations of the Kwanza and Espirito Santo conjugate margins in the South Atlantic as well as of magma-poor margins globally.

1. Introduction

Structural interpretations of seismic profiles have incorporated the concept of polyphase rifting (e.g., Lavier & Manatschal, 2006; Manatschal, 2004; Whitmarsh et al., 2001) to identify the extensional structures formed before and while the crust is extended to the point of break-up (hyperextension). These interpretations also served to check the validity of and improve upon the first polyphase models of rifting (e.g., McIntosh et al., 2014; Péron-Pinvidic & Manatschal, 2009; Savva et al., 2013; Sutra et al., 2013; Unternehr et al., 2010; Van Avendonk et al., 2009). At many margins, hyperextension (i.e., the crust thins to ≤10km) precedes the transition to seafloor spreading. Observations show that slow extension (<20 mm/year), exhumed subcontinental mantle, highly attenuated continental crust, and low magmatic budgets are common characteristics of hyperextended margins (e.g., Brune et al., 2016; Clark, 2018; Franke, 2013; Naliboff et al., 2018; Ros et al., 2017; Sutra et al., 2013; Tugend et al., 2014). By now, many hyperextended domain have been described: Iberian margin (Boillot et al., 1987; Péron-Pinvidic & Manatschal, 2009); Exmouth plateau (Driscoll & Karner, 1998); West African margin (Aslanian et al., 2009; Contrucci et al., 2004; Péron-Pinvidic et al., 2017; Unternehr et al., 2010); mid-Norwegian margin (Osmundsen & Ebbing, 2008); and Australian and Antarctica margins (Ball et al., 2013; Sayers et al., 2001), Pyrenees (Jammes et al., 2009; Masini et al., 2014; Tugend et al., 2014); Alps (Beltrando et al., 2014; Lemoine et al., 1987; Manatschal, 2004; Masini et al., 2012, 2014; Mohn et al., 2010); South China Sea (Lester et al., 2014; McIntosh et al., 2014; Savva et al., 2013).

Hyperextension is associated with the coupling of crustal and mantle Lithosphere deformation since it involves the eventual exhumation of deep crustal material and mantle lithosphere (e.g., Jammes et al., 2009; Manatschal, 2004; Mohn et al., 2010, 2012, 2015; Tugend et al., 2015, 2018). Structural interpretations of many seismic sections (see references above) have distinguished extensional structures that are involved in distributed stretching of the crust and mantle from those that are responsible for coupling crustal and mantle lithosphere deformation. These interpretations separate margins into decoupling domains where deformation in the upper crust in detached form that in the lower crust and mantle (detachment faults); and coupling domains where normal fault zones extend from the crust into the mantle leading to necking (localized thinning; Lavier & Manatschal, 2006) and the eventual exhumation of the lower crust and, in the absence of magma, serpentinized mantle rocks. Understanding the factors controlling decoupling, coupling and hyperextension should provide critical information on the mechanics of lithospheric necking and breakup. This exercise is critical at a time when new thermochronological data of fossil magma-poor margins in the Alps and the Pyrenees have shown that reheating of the crust and the sediments occurs during lithospheric necking (thinning; Smye & Stockli, 2014; Beltrando et al., 2015; Seymour et al., 2016; Hart et al., 2017; Smye et al., 2019). Some authors suggest that these thermal events can be explained by rapid, active mantle upwelling during necking (Smye et al., 2019) and suggest that structures coupling fault in the crust and mantle are linked to both hyperextension and an actively upwelling mantle that could increase heat flow at the base of the extending crust and mantle lithosphere (Chenin et al., 2018; Gallacher et al., 2016; Hart et al., 2017; Huismans & Beaumont, 2008, 2014; Royden & Keen, 1980; Svartman Dias et al., 2015, 2016).

Numerical models can simulate the evolution of magma-poor hyperextended margins for first-order features and be used as experimental tools to test mechanisms by which crustal and mantle deformation becomes coupled or decoupled (e.g., Brune et al., 2014; Chenin et al., 2018; Davis & Lavier, 2017; Huismans & Beaumont, 2007, 2008, 2011; Lavier & Manatschal, 2006; Naliboff et al., 2018; Pérez-Gussinyé & Reston, 2001; Ranéro & Pérez-Gussinyé, 2010; Ros et al., 2017; Svartman Dias et al., 2015, 2016; Van Avendonk et al., 2009). These models did verify that rifting can be polyphase (Lavier & Manatschal, 2006) and involves the thinning of the continental lithosphere by brittle faulting and ductile shearing eventually leading to embrittlement of the whole lithosphere and the coupling of crustal and mantle deformation. However, while a large body of numerical work has grown over the last 20 years to explain the formation and offset of brittle normal faults (e.g., Lavier et al., 1999, 2000), there are few studies dedicated to the mechanics leading to the formation of shear zones decoupling deformation between the crust and the mantle (e.g., Nagel & Buck, 2007; Wu & Lavier, 2016; Nirrengarten et al., 2017; Brune et al., 2017; Naliboff et al., 2018; Korchinski et al., 2018).

Here we propose a new brittle and semibrittle formulation for the formation of normal faults that are rooted in subhorizontal decoupling shear zones that sequentially deform a rheologically layered continental lithosphere from rift initiation to seafloor spreading. The evolution simulates distributed stretching, necking, hyperextension and seafloor spreading and allows for the spontaneous formation of both brittle normal faults and subhorizontal semibrittle shear zones that decouple deformation in the crust from that in the lower crust and mantle lithosphere. In an attempt to check the validity of the simulated mechanism, we compare the resulting tectonic, structural, and thermal evolution to the conjugate margins of Espirito Santo (Brazil) and Kwanza (Angola; Figures 1 and 2). We first present a detailed interpretation of the crustal and sedimentary architecture of the two conjugate margins using long-offset, long record multi-channel seismic reflection profiles. The conjugate seismic profiles were selected based on plate reconstructions (Figure 1; Heine et al., 2013). We then propose a set of numerical experiments aimed at representing the main structural features of the margin to constrain the tectonic, thermal, and rheological evolution of these margins from incipient extension to seafloor spreading.

2. Tectonic Setting

Rifting between the Brazilian Espirito Santo and Campos Basins and the Angolan Kwanza Basin (Figures 1 and 2) occurred in a Precambrian orogenic lithosphere. Rifting was localized between the Angola Block (Paleoproterozoic) and the Cabo Frio Tectonic Domain which was accreted during the Cambrian Ribeira Orogen (~510 Ma; Trouw et al., 2000) and involved the collision of the Angola block with the Brazilian

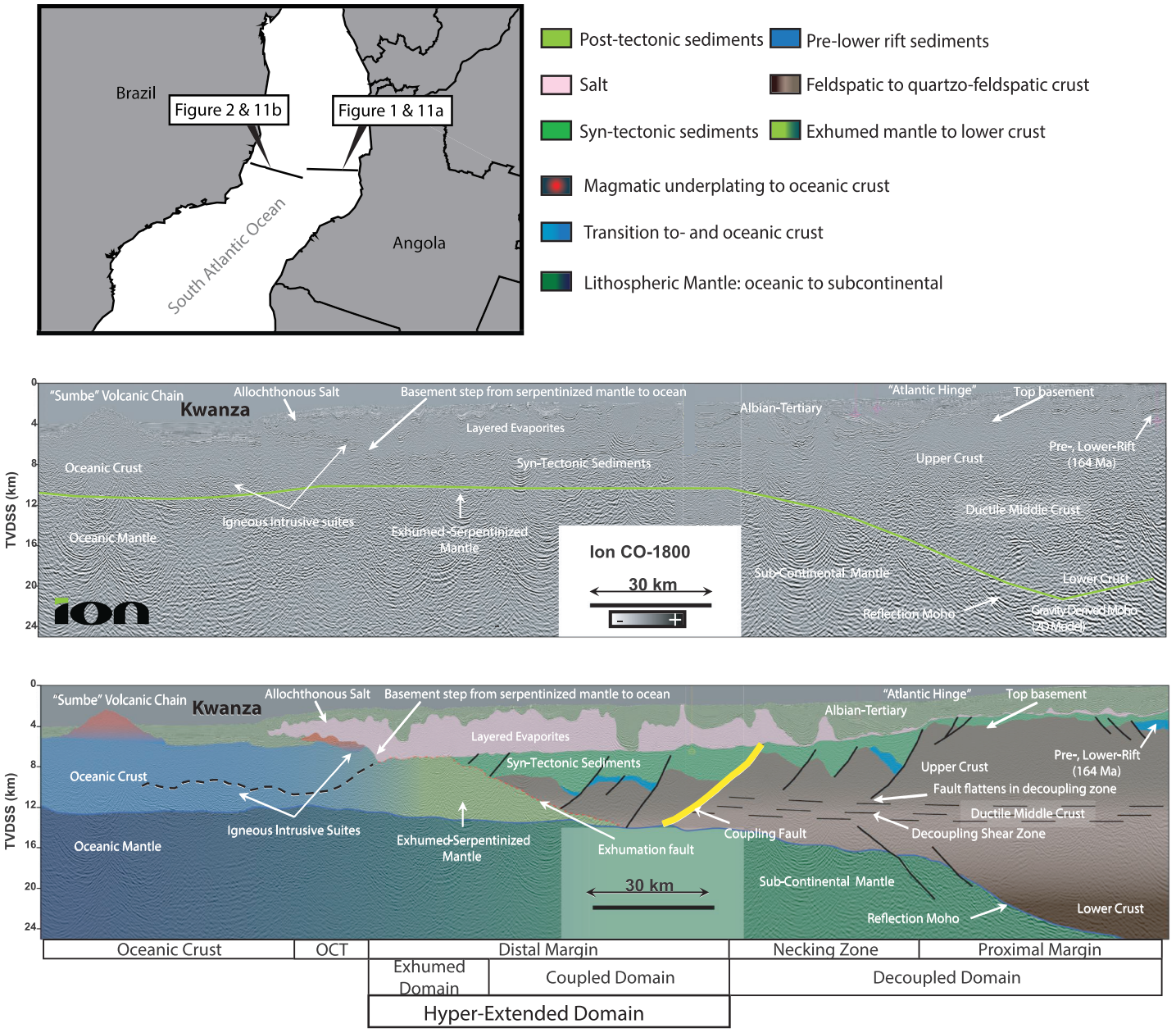

Figure 1. Location map indicates the positions of the Kwanza Espirito Santo sections restored to approximately the end Aptian time (GPlates 2.0, plate restoration using, Heine et al., 2013). This illustrates that the profiles are approximately conjugate. Profile from ION GXT. Schematic section across the Kwanza margin based on drill hole and seismic observations. See legend and text for details. A Moho (green line) from a simple 2-D gravity model is superimposed assuming simplified densities: mantle 3.3 upper crust, 2.75, lower crust 2.9, post-tectonic sediments 2.3–2.4, evaporates 2.3, syntectonic sediments 2.5, and oceanic crust 2.9 g/cm^3.

Oriental Terrain (Kröner & Stern, 2004; Schmitt et al., 2016). The Cretaceous breakup did not occur along the suture of the Ribera orogen, but was located dominantly toward the Angola block (figure 8 in Schmitt et al., 2016). The resulting split led to the accreted Ribera terrains, arcs, syncollisional, and post collisional plutons remaining on the Brazilian margin (Schmitt et al., 2016).

Rifting in the South Atlantic initiated in the Berriasian (~145 Ma) and continued through the late Aptian (110 Ma). While the exact ages of rifting and breakup are still debated, several phases of rifting have been identified in the stratigraphic record. The first phase corresponds mainly to large basement involved faults

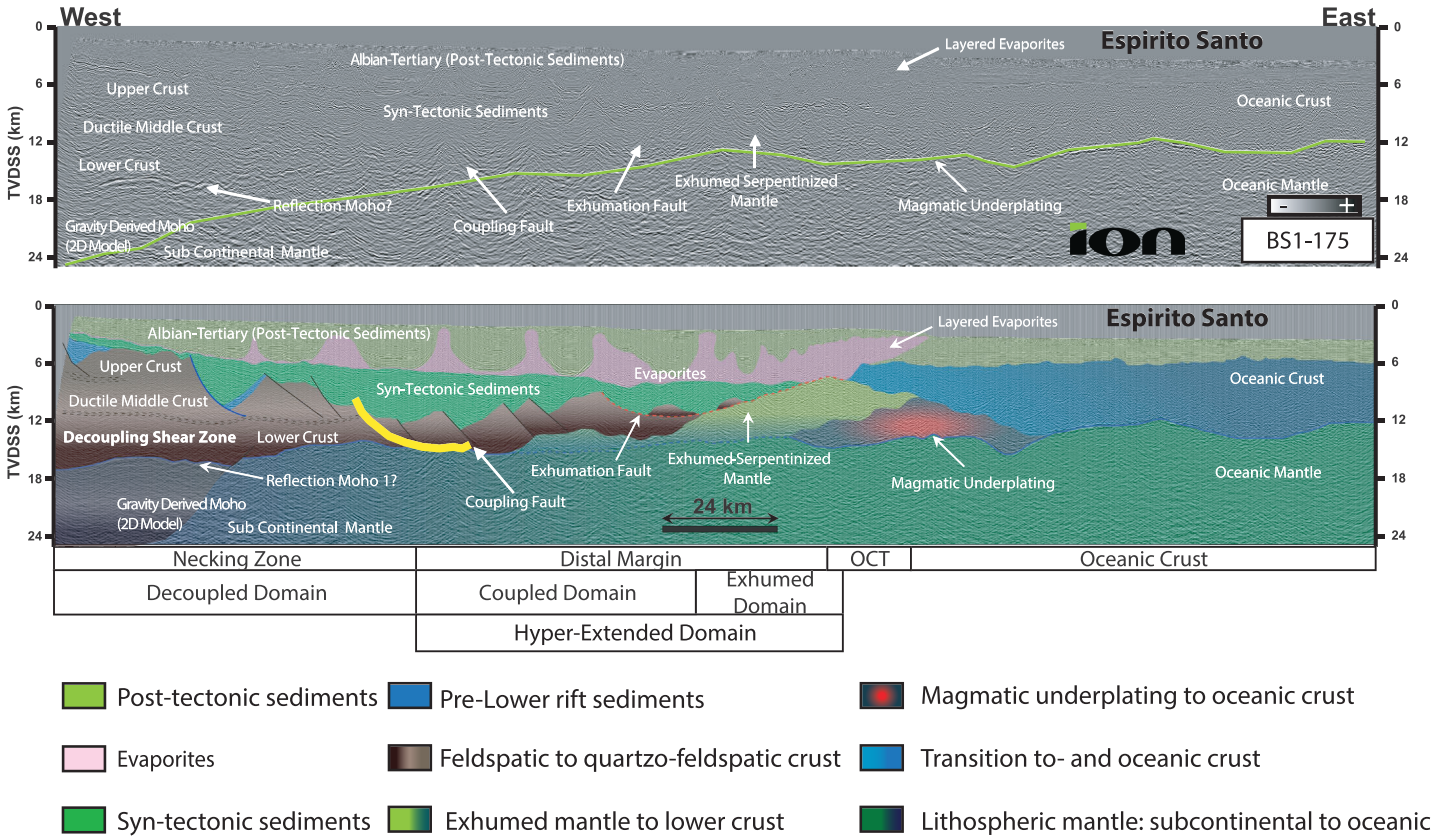

Figure 2. Schematic section across the Espirito Santo margin inspired by seismic observations. See legend and text for details. Profile from Ion GXT. A Moho (green line) from a simple 2-D gravity model is superimposed assuming simplified densities: mantle 3.3 upper crust, 2.75, lower crust 2.9, post-tectonic sediments 2.3–2.4, evaporates 2.3, syntectonic sediments 2.5, and oceanic crust 2.9 g/cm3.

with lacustrine early syntectonic sediments from the Berriasian to Mid-Barremian (145–127 Ma). Within or prior to the formation of these basins tholeiitic basalts have been identified in the pre-tectonic to early syntectonic phase. These volcanics may represent the northernmost extent of the Paraná-Etendeka flood basalts and were erupted very rapidly at 133 ± 1 Ma (Stewart et al., 1996). The basalts are commonly interpreted to be related to a plume (e.g., Guardado et al., 1990; Karner & Gambôa, 2007).

The early syntectonic phase, which significantly thinned the crust, led to mantle exhumation during the late-Aptian (approximately 127–112Ma). It is during this stage that a sag basin is formed, preceding the fast deposition of a syntectonic salt layer, which is interpreted to has been deposited directly onto exhumed mantle (e.g., Péron-Pinvidic et al., 2017). Many recent studies have focused on mapping and modeling this late phase of rifting recorded in the transition between the continental and oceanic domains (e.g., Blaich et al., 2011; Contrucci et al., 2004; Cowie et al., 2017; Moulin et al., 2005; Torsvik et al., 2009; Unternehr et al., 2010).

Lithospheric breakup is inferred to occur at about 112 to 110 Ma (e.g., Davison, 1999; Karner et al., 2003; Moulin et al., 2005; Moulin et al., 2010; Torsvik et al., 2009). The exact timing of breakup remains hard to determine north of the Walvis Ridge because there are no identified magnetic anomalies due to the transition from rifting to seafloor spreading occurs during the Cretaceous Normal Superchron, CNS, 83.5–120.6 Ma (Gaina et al., 2013). While there is some uncertainty in the location and the age of breakup, all models agree that breakup is diachronous from south to north. Recently, Heine et al. (2013) proposed a revision of the age of the transition to seafloor spreading to 119 Ma between the Campos and Kwanza basins. Brune et al. (2014) assumed rifting rates along the Kwanza Basin to vary from 1.0 cm/year in the south to 0.4 cm/year in the north along the Angola-Gabon border. To be consistent with previous work, an extension rate of 1.0 cm/year is estimated based on the plate model of Heine et al. (2013).

3. Conjugate Margin Profiles

We adopted the modified rift domain approach presented by Sutra et al. (2013) for the interpretation of the profiles. Rift domains, decoupled (stretching and necking), hyperextended (coupled and exhumed), and the oceanic crust has been defined and mapped across our assumed conjugate margin profiles (Figure 1).

3.1. Kwanza Basin Offshore Angola

3.1.1. Stretching Domain

The existing seismic coverage does not include the nearshore and onshore portions of the stretching domain. Therefore, the total width of the stretching area is unknown. Immediately landward of the Atlantic hinge, a small graben structure is interpreted but it does not significantly modify the crustal structure as very little extension is accommodated there. A key observation that suggests that the crust is not considerably thinned there (~23 km thick).

3.1.2. Necking Zone

Within the necking domain, significant basinward dipping normal faults are observed, which appear to sole-out within the crust (Figure 1). At depth, dipping seismic reflectors are observed, and a Moho reflector is interpreted to shallow from ~25 km to ~15 km (Figure 1). Within the necking zone, the fourth fault (highlighted in yellow) is interpreted to breach the middle crust, intersect Moho, and penetrate mantle (Figure 1). This fault is interpreted as the coupling fault because it roots in the mantle lithosphere and to couple extension in the upper crust with deformation in the mantle lithosphere. The necking zone shown in the profile is ~30 km wide (Figure 1).

3.1.3. Hyperextended Domain and Ocean Continent Transition

Oceanward of the necking zone, we interpret a hyperextended domain. Within this domain, extensive oceanward dipping faults are interpreted to transect the ≤10-km-thick crust and penetrate the mantle. The Moho is construed to uplift along the coupling fault until it intersects the base of salt (Figure 1). As already pointed out by Péron-Pinvidic et al. (2017), this structural characteristic allows us to approximately date mantle exhumation as synevaporite in age, suggesting that both exhumation and evaporite deposition in Angola were synchronous. Gravity modeling for crustal thickness within this domain suggests a crust that is 4–5 km thick and based on the seismic interpretation it is inferred to consist at least partly of serpentinized mantle. The hyperextended crust/domain, including the exhumed mantle, is ~60km wide (Figure 1). The depth of the top of the interpreted exhumed mantle is 1 km deeper than the top of oceanic crust to the west. The 1- to 2-km step-up in basement is interpreted to represent the juxtaposition of average thickness oceanic crust (about 6–7 km) against the thinner crust with or without exhumed mantle including magmatic additions. The transition into oceanic crust also coincides with the point where the evaporites are interpreted to become allochthonous (Duval et al., 1992). The basement step also coincides with interpreted volcanic flows. The timing of the volcanic flows is, therefore, synbreakup to postbreakup. The close association and possible inter-fingering of the allochthonous evaporites with magma suggest the volcanism outlasts continental breakup, and that salt continued to flow after the breakup, forming the allochthon above the oceanic crust.

3.1.4. Oceanic Domain

Moho is not clearly imaged within the oceanic domain. This feature may be because the oceanic crust has been thickened as a result of postbreakup magmatic additions associated with the Cenozoic Sumbe volcanic chain (e.g., Marzoli et al., 1999). While the image of the volcano is impressive, it is a postbreakup event and is not related to the rifting, breakup, or thermal relaxation processes.

3.2. Espirito Santo Basin Offshore Brazil

3.2.1. Stretching Domain

The seismic section does not cover the nearshore and onshore portions of the stretching domain. Therefore, the width of the stretching region on the Brazil side remains unknown. At the western edge of the seismic line, listric normal faults rooted in a subhorizontal high amplitude reflector at ~18-km depth in the middle crust are interpreted as shear zones decoupling deformation between the upper and lower crust (Figure 2). The seismic Moho is, however not well imaged, and we cannot exclude that the flat reflector at ~18 km is a seismic Moho: however, this interpretation is not favored since the isostatic response to the corresponding amount of crustal thinning (about 50%) would force the top basement reflector to be located at 10 to 12-km depth instead of 5 to 6 km as is observed westward of the necking zone (Figure 2). We propose a

deeper, poorly imaged Moho at 24–25 km. This Moho is consistent with a simple 2-D gravity model derived Moho and the expected isostatic response of the Lithosphere. We therefore suggest that the shallower reflector is the top of the lower crust and a decoupling shear zone.

3.2.2. Necking Zone

The extensional structures interpreted within the westernmost part of the line in the upper crust sole out within the crust. The assumption of a deeper Moho results in a strong necking, which is coincident with the first sizeable half-graben basin. The oceanward, distal, border of the necking zone is delineated by the presence of a coupling fault, which is interpreted to cross from the upper crust to the Moho, coupling rifting processes. The interpretation results in a necking zone that is ~50 km wide that is delimited by the coupling fault. The hyperextended area is ~75 km wide and consists of a coupled and exhumed domain. Within the coupled domain the crust is interpreted to be 10 to 3 km thick, with detachment faults that are rooted in shallow subhorizontal shear zones at the base of the continental crust. To the east, the oceanic crust bounds the exhumed mantle zone. The transition to the oceanic domain is interpreted to be where the seismic basement steps up 1–2 km. The average thickness of the oceanic crust is ~6 km, although locally it may be thicker at the interpreted continental-ocean boundary, where we assume that a posttectonic magmatic event thickened the crust.

3.2.3. Hyperextended Domain and Ocean Continent Transition

The exhumed mantle is associated with a crust that is interpreted to be initially 4–5 km thick (Figure 2). As in Angola, the exhumed mantle appears to be contemporaneous with the presence of evaporates and locally also magma. We interpret this salt as being allochthonous (Duval et al., 1992) and being coincident with an upward step in basement between the interpreted serpentinized mantle domain and the oceanic crust to the west. An extensional detachment fault is believed to provide the mechanism for exhuming the mantle (dashed red line Figure 2). We interpret a landward dipping reflector at a depth of approximately 12 km that represents the serpentinization front. A deeper, second prominent seismic reflector is detected corresponding to the oceanward equivalent of the oceanic Moho. This second reflector is the base of the present-day crust within the exhumed domain. It represents an underplating magmatic body that is of postbreakup age, and that thickened the crust.

3.2.4. Oceanic Domain

Oceanward, normal thickness oceanic crust (6–7 km) is reached within ~25 km and we assume that steady-state seafloor spreading is achieved. Therefore, the posttectonic magmatic event is thought to have occurred shortly after seafloor spreading processes occurred, due to its limited lateral distribution across the margin. However, it could also be related to the younger Abrolios magmatic event in the Eocene (Oliveira et al., 2018).

4. Uncertainties on the Interpretations of the Kwanza and Espirito-Santos Profile Interpretations

Simplified 2-D gravity models complement the interpretation to establish the first-order architecture of the margin; however, gravity models are not able to differentiate the key details or to reduce the uncertainty of the processes inferred, in particular for the lithologies. Therefore, as already acknowledged, the seismic reflection data do not correctly image the composition of the crust within the hyperextended domain leading to some interpretational uncertainty across both the Angolan and Brazilian lines. The interpretations provided in the previous paragraphs are non-unique, and we are aware of the limitations provided by the data as indicated above (cf. Peron-Pinvidic et al., 2018; Van Avendonk et al., 2009; Péron-Pinvidic & Manatschal, 2009). It is possible to assume that the crust did not go through hyperextension oceanward of the necking zone and that the ocean continent transition (OCT) is magmatic. Such a model was proposed for the Santos Basin by Evain et al. (2015) on a segment more closely associated with plume/transform activity of the South Atlantic margin that the one studied here. Alternatively, the crust could be interpreted as proto-oceanic or oceanic, which would impose early and broad oceanic crustal domains in the south Atlantic (e.g., Jackson et al., 2000). Our interpretations, therefore, represent end-member representations of the Kwanza and Espirito Santo conjugate margins that in 2-D appear to be valid. In 3-D or along strike, the structural characteristics are likely to change substantially. Future studies will need to address the along-strike variability and the uncertainty of the interpretation of the crustal architecture of the margin. Access to industry 3-D sets, including drill hole data, that are not in the

open literature domain, will be necessary to describe the along-strike variations and evolution of these domains, which at present is not possible. Given the uncertainties, we are not explicitly describing the mineral composition of the rocks forming the hyperextended domain, since the velocities and densities of hydrated crustal, magmatic and mantle rocks are overlapping and cannot be distinguished without additional data, well control and sampling. Another significant assumption is that there is an oceanward younging of the detachments in the hyperextended domain that is unresolved with the existing long offset 2-D data. Finally, both margins reveal evidence of posttectonic magmatism, although at present the onset of the postrift magmatism is unconstrained. The result is that both margins show thickened posttectonic magmatism, possibly related to the Sumbe volcanic chain and the Abrolios magmatic system for the two margins respectively. This final point is crucial because it also highlights that when interpreting rifted margins, one needs to be aware that the present geometry may not fully reflect the syntectonic structure of the margin because posttectonic processes can modify and mask the original margin geometry. This additional uncertainty also needs to be acknowledged.

5. Comparison of the Kwanza and Espirito-Santos Profile Interpretations

Based on the interpretations presented above, it is noteworthy that there are several first-order observations and similarities between the conjugate Kwanza and the Espirito Santos profiles. (1) The presence of a decoupled domain where basement faults decouple from lower crust deformation within the continental crust (Figures 1 and 2). (2) Both margins have necking zones where the crust thins basinward. However, the necking is not symmetric, and in the Espirito-Santos profile, the necking zone is interpreted to be ~50 km wide, while in the Kwanza profile it is only ~30 km. (3) The basinward boundary of the necking domain is interpreted to be bounded by a basement fault (coupling fault) that roots within the lithospheric mantle. We observe along both margins that the basin bounded by the coupling fault is, in fact, the thickest within the distal margin, where, pre-salt, synrift sediments are up to 6–7 km thick, reaching their maximal thickness. (4) Both margins, are interpreted to have a coupled and an exhumed domain and a 1- to 2-km basement step-up/ramp at the transition toward oceanic crust. While the exhumed domain is relatively symmetric, although ill-defined, the coupled area is wider in the Espirito Santo basin. (5) Regarding kinematic constraints, the interpreted exhumation domains across both margins are contemporaneous with the salt deposition, therefore, indicating that in the scenario presented here, exhumation had to occur between 116 and 111 Ma, which is the age of the salt (Davison, 2007; Dias et al., 1994). However, recent studies put some doubt on the age and onset of salt deposition within the South Atlantic (e.g., Tedeschi et al., 2017), suggesting the evaporites were deposited earlier during the early Aptian Oceanic Anoxic Event 1a interval. The age of the Oceanic Anoxic Event 1a can vary depending on the stratigraphic timescale used ranging from 119–120 Ma to 125 Ma (Jenkyns, 2018, and references therein). Therefore, it is within these additional stratigraphic, depositional and tectonic uncertainties that our analysis is bound.

6. Rheological Conditions

To clarify the terminology in this paper, we will distinguish four types of extensional structures: (1) “Normal faults” that localize in a brittle crust and mantle at high dip-angle (>50°) and can flexurally rotate to low-angle with large offset (e.g., Lavier et al., 1999). (2) “Decoupling extensional shear zones” that are subhorizontal “mixed” brittle-ductile shear zones initiated in the brittle-ductile transition (BDT) in semibrittle material (semibrittle material; e.g., Mohn et al., 2015). (3) “Listric normal faults” that form at high dip-angle in the brittle layer and rotate to a subhorizontal dip at the BDT when rooted in a subhorizontal brittle-ductile shear zone. (4) “Coupling faults” that initially form and extend at high dip-angle through the brittle crust, the BDT, and the brittle mantle. Over time, these structures exhume material originating from the middle and lower crust and after enough necking serpentinized mantle.

To simulate localization of extensional structures during rifting, inherited structures, strain and strain rate formulations have been used to parameterize viscous softening and the formation of semibrittle and ductile shear zones (Huismans & Beaumont, 2003; Lavier & Manatschal, 2006; Regenauer-Lieb et al., 2006; Nagel & Buck, 2007; Weinberg et al., 2007). While dynamic models, including this type of rheological parameterization, can model the long-term evolution of rifts, they are first-order approximations of the dominant weakening process leading to the formation of extensional structures. Kinematic models, however, are

constrained by geological and geophysical observations and can provide useful insights in the tectonic processes involved in the creation of extensional structures (e.g., Kusznir et al., 1991; Mohn et al., 2015; Ranéro & Pérez-Gussinyé, 2010). Some of these models include polyphase faulting (Mohn et al., 2015; Ranéro & Pérez-Gussinyé, 2010; Reston, 2007), lower crustal flow toward and away from the necking zone (Brun & Beslier, 1996; Karner et al., 2003). Polyphase faulting models assume that several generations of normal faults progressively thin the crust in the same crustal block in the brittle domain (Ranéro & Pérez-Gussinyé, 2010). Ranéro and Pérez-Gussinyé (2010) proposed a technique to palinspastically reconstruct normal faulting such that the amount of thinning is consistent with the observed normal fault offsets. This method assumes that brittle faults in the upper crust extend and widen progressively into the ductile lower crust. After an increment of extension, the resulting brittle (upper crust) and ductile (lower crust) deformation are balanced with the increase in extension. Even though the choice of deformation mechanism is strictly kinematic, they suggest that strain in the BDT and the lower crust occurs over relatively narrow zones that may correspond to brittle-ductile shear zones.

With laboratory experiments, field observations, and numerical experiments, these studies are slowly changing our understanding of the yield strength at the BDT. The commonly held view is that the strength profile is following the yield stress envelope proposed by Goetze and Evans (1979). The use of the YSE approximation follows from earlier works developed to constrain the rheology of the oceanic and continental lithosphere through computing the elastic strength (Watts, 2002 and references therein). According to this model, deformation in the upper crust occurs by brittle faulting and deformation in the lower crust occurs by ductile flow with an abrupt transition from brittle to ductile behavior. In this representation, no strain localization occurs at the BDT, and deformation is delocalized in the middle and lower crust. However, laboratory experiments of rock deformation and field observations suggest that the BDT is very progressive and that deformation there is localized in shear zones of finite width (e.g., Bürgmann & Dresen, 2008; Davis et al., 1986; Kohlstedt et al., 1995; Scholz, 2002). The presence of fluids, the polymineralic nature of rocks and the fact that brittle and ductile phases coexist in a mixed brittle-ductile (semibrittle) material render estimates of the thickness and the strength of the BDT difficult (e.g., Handy, 1990; Jammes et al., 2015; Lavier et al., 2013).

Moreover, the record of the deformation processes is often so complicated that deciphering the principal mechanisms responsible for localization is arduous. For example, a strong brittle feldspathic mineral phase coexists with a weak ductile quartz phase at the pressure and temperature conditions of the greenschist metamorphic facies (e.g., Scholz, 2002) and can lead to the formation of wider, yet localized shear zone at the BDT over a wide range of temperature conditions and compositions (e.g., Jammes et al., 2015). When a significant strength contrast exists between the different mineral phases at the BDT, structural weakening is likely to occur, as shown by Duretz et al. (2016). However, other weakening mechanisms may dominate the localization process. These include cohesion loss (Jammes et al., 2015), grain size reduction (Scholz, 2002; Sibson, 1977), and compositional weakening due to metamorphic and hydration reactions associated with the formation of fracture networks (e.g., Holyoke & Tullis, 2006; Kjøll et al., 2015; Kronenberg et al., 1990; Lavier et al., 2013; Stipp et al., 2002 and references therein).

Rocks from hyperextended domains have only been drilled along the Iberia-Newfoundland margins (ODP Legs 103, 149, 173 & 210) or have been observed as parts of fossil margins in collisional orogens (e.g., Tethys margin in the Alps (Manatschal, 2004; Manatschal & Bernoulli, 1999; Mohn et al., 2012). For margins, the deformation mechanisms associated with the formation of normal faults, listric normal faults, decoupling shear zones and coupling faults are observed at the outcrop scale in the Alps and the Pyrenees and at the scale of seismic sections. The rocks in these outcrops of exhumed fossil rift show evidence for pervasive hydration reactions, including the breakdown of feldspar and olivine to clay minerals and serpentine, respectively (e.g., Bertotti et al., 1993; Handy & Stünitz, 2002; Jammes et al., 2009; Manatschal, 2004; Manatschal & Bernoulli, 1999; Masini et al., 2012, 2014; Mohn et al., 2010, 2012; Osmundsen & Ebbing, 2008; Péron-Pinvidic & Manatschal, 2009; Ranéro & Pérez-Gussinyé, 2010). The resulting localization of deformation is therefore fluid assisted (Handy & Stünitz, 2002). In the outcrops of exhumed mantle, the mechanism of deformation involved reaction weakening through the transformation of olivine to serpentine, in response serpentine cataclasites are formed along discrete anastomosing shear zones (Handy & Stünitz, 2002; Manatschal & Bernoulli, 1999). In the crust, normal faults, listric normal faults decoupling shear zones form under greenschist conditions are likely associated with compositional weakening caused

by the precipitation of quartz from fluids in synextensional fractures or due to the breakdown of feldspars to fine grain mica or epidote (sericitization, saussuritization; e.g., Mohn et al., 2012, Wintsch et al., 1995 for the fossil Thetyan margin). These processes can be associated with the formation of anastomosing, cataclastic or mylonitic shear zones (Lavier et al., 2013 and references therein), occur typically in the BDT and can result in large-scale ductile shear zones decoupling the upper and lower crust (e.g., the decoupling shear zone, Eita shear zone in Mohn et al., 2012). These observations are comparable to those made in the Basin and Range province (mylonitic front; Davis et al., 1986) or the brittle-ductile transition in the hyperextended crust (e.g., Manatschal et al., 2001). This suggests that throughout different pressure and temperature conditions brittle and ductile processes are interacting to localize deformation within decoupling levels, which evolve through time as the rifting progresses toward breakup. This type of brittle-ductile deformation has been described in environments where fluids or compositional contrasts are present (e.g., Handy, 1990; Mancktelow & Pennachioni, 2005). We believe that such processes are dominant in hyperextended domains where hydrothermal circulation and an unlimited reservoir of fluids are present. During reaction or compositional weakening, softening occurs when a weak viscous phase populates fractures in a damaged zone. Here damage corresponds to the accumulated strain needed to form a network of fractures. When enough dissipation occurred, the damaged zone is populated by a weak viscous phase likely aided by a fluid releasing mechanism (e.g., Lavier et al., 2013; Mancktelow & Pennachioni, 2005). We implicitly state that enough work was done to create a damaged zone that is permeable to fluid migration. For this phenomenon to occur, an initially strong phase is needed to enable brittle damage. Eventually, through the generation of weaker mineral phases, the initial strong phase coexists with a mobile weaker phase at the same pressure and temperature (e.g., coexistence of brittle feldspar and wet quartz; Handy, 1990; Lavier et al., 2013; Jammes et al., 2015; Jammes & Lavier, 2016, 2019).

Interestingly, while elastoplastic and viscoelastic flow approximations can be used to simulate brittle and ductile deformation in the lithosphere, no explicit flow laws exist for semibrittle materials where both brittle and ductile behavior coexist. Regardless of the success of any of the use of dislocation and diffusion creep laws in models of tectonic deformation (e.g., Burov & Poliakov, 2001), how deformation accumulates in the semibrittle crust is still unresolved. To model compositional weakening in a semibrittle media, we develop a rheological parameterization by updating the approach used by Lavier and Manatschal (2006).

7. Constitutive Update for the Formation of Semibrittle Fault Systems and Ductile Shear Zones in the Continental Crust and the Serpentinized Mantlef

In our semibrittle model, plastic work (nonrecoverable) is accumulated as both inelastic plastic (Mohr-Coulomb) and viscous work (dislocation creep). Our yield criterion for compositional weakening is a convenient extension of Freudenthal's critical plastic work criterion (Freudenthal, 1950) that depends on both the square root of the second invariant of stress, σ^{II} and strain, ε^{II} (also called Mises stress and strain):

$$\int_0^{\varepsilon_c^{II}} \sigma^{II}\, d\varepsilon^{II} \geq C \tag{1}$$

where ε_c^{II}, is the critical strain (square root of the second invariant the sum of the viscous and plastic strain) at which semibrittle fractures are populated by the weak viscous phase. C is a constant in Joules. By defining work in this way, we define a frame independent criterion. We therefore define a yield work rather than a yield stress that allows for localization over a range of depth and temperature in the lithosphere. We assume that the time scale of weakening is instantaneous compared to geological time scales. We can also assume that the stresses are constant over the time of damage zone formation and work dissipation. The yield criterion becomes:

$$\sigma_y^{II}\, \varepsilon_c^{II} \geq C \tag{2}$$

When assuming pressure dependent Mohr-Coulomb plastic behavior for the brittle crust and viscous creep for the ductile crust, one can plot the yield stress envelope as a function of depth for a given geotherm (e.g., Kohlstedt et al., 1995). We assumed that the yield stress for semibrittle fractures is dependent on critical work and accumulated strain. We can extend the principle of the yield stress envelope by plotting our semibrittle yield criterion as yield stress as a function of total strain (Figure 3). To have a consistent yield stress

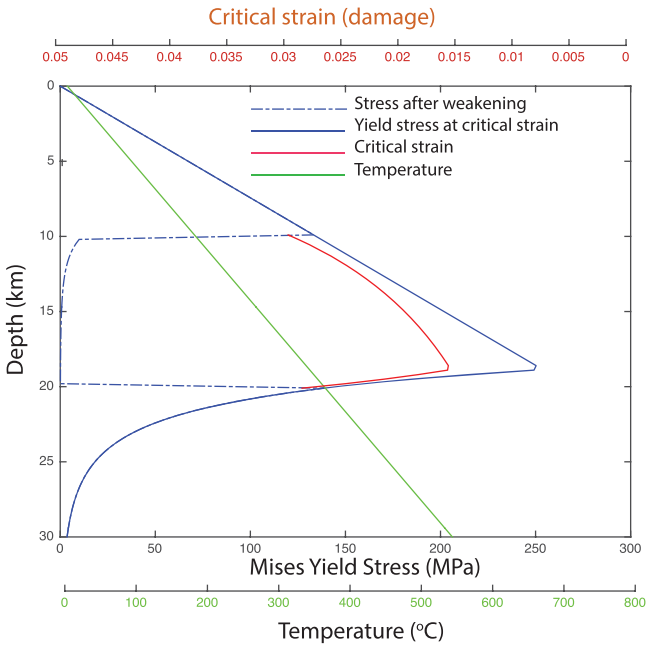

Figure 3. Yield stress envelope including the semibrittle damage transition for a work $W = 4.10^6$ J. Before weakening (continuous blue line) the middle crust is brittle. After weakening (blue dot dash line) the middle crust is behaving in a semibrittle manner. The curve in green in the assumed geotherm in the crust for this yield stress envelope. In red is the critical strain variation between 200 and 350 °C given in equation (2) using $C = 10^7$ J. In blue in the corresponding yield stress for the critical strain calculated in the red curve. The blue dash-dotted line represents the yield stress after the material transition from dry plagioclase to wet quartz (Rybacki et al., 2008, 2010).

between Mohr-Coulomb, viscous creep and ductile fracture, we calculate the Mises stress, σ^{II} for Mohr Coulomb and viscous creep at yield. Mohr Coulomb shear stress, τ at yield is defined as:

$$\tau = \mu\sigma_n \tag{3}$$

where σ_n is the normal stress, μ the static friction coefficient. In 2-D the second invariant of the stress at yield is defined as a function of the principal stresses as:

$$\sigma_y^{II} = \sqrt{\sigma_1\sigma_3} \tag{4}$$

or as a function of shear stress at yield, with $\sigma_n = (\sigma_1+\sigma_3)/2$ and $\tau = (\sigma_1 - \sigma_3)/2$.

$$\sigma_y^{II} = \sqrt{\tau^2\left(\frac{1-\mu}{\mu}\right)} \tag{5}$$

For dislocation creep the second invariant at yield is defined as follow:

$$\sigma_y^{II} = A\left(\dot{\varepsilon}^{II}\right)^{\left(1-\frac{1}{n}\right)} e^{\left(\frac{Q}{nR(T+273)}\right)} \tag{6}$$

where A is the creep law pre-exponent, $\dot{\varepsilon}^{II}$ the square root of the second invariant of the strain rate, n the creep law exponent, R the gas constant and T the temperature. Finally, the yield stress for fracture is defined as:

$$\sigma_y^{II} = \frac{C}{\varepsilon_c^{II}} \tag{7}$$

We assume the fluid is present in the host rock when the depth is shallow enough (<15 km) for the circulation of meteoric fluids (Fricke et al., 1992). For the case of mantle serpentinization, we assume that it is limited by

temperature (T < 400 °C) at a depth less than 15 km. When these conditions are met, we replace dry olivine mantle by serpentinized mantle. We use a friction coefficient of 0.01 to simulate a weak serpentinized mantle under high pore fluid pressure (Hilairet et al., 2007). Observations of exhumed serpentinized mantle in the Alps (Pinto et al., 2015) show that mantle serpentinization is of the order of 60%, and we decrease the density accordingly. For the continental crust, feldspar and wet quartz rheology are controlled by dislocation creep laws (Rybacki et al., 2008, 2010) with a minimum viscosity of 10^{19} Pa.s. We plot yield stress as a function of depth (Figure 3) for a friction coefficient of 0.6 and a dislocation creep law for plagioclase for a constant strain rate of $\dot{\varepsilon} = 10^{-14}$/s, a linear geotherm of 18.33 °C/km (550 °C at 30-km depth) and $C = 10^7$ J, a value that corresponds to a yield at a stress of ~125 MPa for a Mises strain of ~3% or 90 MPa for 4%. The defined rheology a damaged zone (plastic strain) at the brittle ductile transition that coalesce into ductile shear zones. In the brittle part of the crust these zones form as shear fractures following the Mohr-Coulomb orientation for localization. In the ductile crust the fractures form in the direction of the maximum shear stress. Both types of fractures are then deforming in a ductile manner after a time, t_M corresponding to the initial viscoelastic response of a Maxwell body. In addition to defining a yield for work, we restrict yield to temperatures between 200 and 350 °C to correspond to the onset of quartz ductility and that of plagioclase, respectively. This range is the crustal semibrittle domain where brittle plagioclase coexists with ductile quartz.

8. Models of Hyperextended Margins

8.1. Model setup

To test our new numerical parameterization, we chose to simulate the tectonic, sedimentary and thermal evolution of the two cross sections of the conjugate margins of Kwanza and Espirito Santo (Figures 1 and 2). We assume that the rift initiated in lithosphere formed during the Pan African orogeny that ended in the Proterozoic (~510 Ma; Schmitt et al., 2016). We therefore use an initial thermal age of 500 Myr for the lithosphere, with a 114-km lithospheric thickness (Svartman Dias et al., 2015) and we assume a constant rate of extension of 1 cm/year total rate (as was adopted by Brune et al., 2014 from Heine et al., 2013 half-rates) While the spreading rates probably varied temporally and spatially along the margin, this is a reasonable approximation compared to rates extracted from recent plate models for the South Atlantic models (Gaina et al., 2013; Heine et al., 2013). We assume that the initial crustal thickness is 33 km and that the base of the lithosphere is at a 114-km depth that corresponds to the base of our model, where isostatic equilibrium is enforced with a Winkler type foundation (it is underlain by an inviscid fluid asthenosphere of fixed density = 3170 kg/m^3; Burov & Poliakov, 2001). At the surface, water loading is applied where the nodes of the model are below sea level. Above sea level the nodes are free (air). The temperature at the surface and at the base of the lithosphere is fixed to 20 °C above water (4 °C below water) and 1330 °C, respectively and no heat-flow boundary conditions are set at the sides of the model. The initial box size is 200 km in width by 114 km in depth. As deformation proceeds the box width increases and we fix the bottom of the lithosphere at 114 km. Asthenospheric material crossing this boundary is set at 1330 °C and becomes part of the thermally diffusive and advective (in the Lagrangian meaning) lithosphere. The numerical technique used is identical to that described in Lavier and Manatschal (2006), Tan et al. (2012) and Svartman Dias et al. (2015).

8.2. Erosion and Sedimentation

Sedimentation and erosion can significantly affect the thermal structure and therefore the tectonic processes at continental rifts. The weight of the sediments that fills the rift basin depresses the crust and lithosphere. The filling of the accommodation space and low thermal conductivity of clastic sediments decreases heat flow and raises the isotherms in the crust. Erosion has the opposite effect. The mass removal creates structural exhumation that can be several times larger than the tectonic uplift (Garfunkel, 1988; Watts, 2002). Erosion and sedimentation transport are modeled with a diffusive formulation and deposition is modeled as a source term in the diffusion equation for sediments. Some transport of sediments occurs by the advection of the grid in the Lagrangian grid. The equation is therefore:

$$\frac{\partial h}{\partial t} = k\frac{\partial^2 h}{\partial x^2} + S_x \tag{8}$$

where k is the diffusivity of the sediments in m^2/s and S_x is the source for the deposition of sediments, x is the horizontal direction and h the topography. k varies whether the sediments are under water ($k = 10^{-7}$ m^2.s) or

above sea level ($k = 5 \times 10^{-7}$ m^2/s). We did not vary the erosional parameters to study their effect on the thermomechanical evolution of the margin. Instead, S_x is calculated to approximately match the amount of sediments deposited in Kwanza and Espirito Santo (~4 km) in addition to that distributed by the diffusion of topography. If the sediments are below sea level they are water loaded and compacted following Atty's law for standard siliciclastic sediments (Allen & Allen, 2013). The salt is modeled as a low constant viscosity Maxwell viscoelastic fluid (10^{19} Pa.s), with low density (2100 kg/m^3) and of high thermal conductivity ($4\,W \cdot m^{-1} \cdot K^{-1}$). It is initially deposited at a rate of 1000 m to 3,000 m per Myr at water depth sallower than 10 m consistent with geological constraints (Tedeshi et al., 2017). The salt deposits in the shallow part of the margin and flows viscously under the effect of the gravity potentials generated by the basin topographic highs and lows. The salt's high thermal conductivity increases the surface heat flow after deposition. This cools the siliciclastic sediments and crust below the salt basins.

8.3. Volcanic Underplating and Accretion of Oceanic Crust

The local temperature increases and change in density accompanying magmatic underplating and the formation of oceanic crust is likely to have a large effect on the thermal and subsidence history of the conjugate margins. Here we propose a kinematic scheme to simulate the emplacement of magmatic additions and the formation of oceanic crust that is set to approximately match the observations (Figures 1 and 2). It allows the model to capture the physical effects of density change, and the emplacement near the surface of high temperature igneous rocks. In addition to the modeling of serpentinization this technique provides us with a first order representation of the OCT for the given interpretations. The formation of oceanic crust is simulated in a way similar to that of Buck et al. (2005) with the additional assumptions that: (1) accretion in the lithospheric mantle is initiated to approximately form the underplated bodies and the oceanic crust interpreted from the seismic data. It corresponds approximately to the time when the 1250 °C isotherm reaches 40-km depth; (2) the accretion of magmatic material occurs in the uppermost mantle lithosphere. These conditions allow for accretion of magma both at the base of the continental and the oceanic crust and at the seafloor. Mantle exhumation occurs when the subcontinental mantle reaches a depth less than 10 km and the 1250 °C is at a depth greater than 40 km. Numerical models of melt production during rifting (Davis & Lavier, 2017) show that melt production is initiated around 100 to 80 km in a weak viscoelastic asthenosphere. However, to allow rapid migration though dikes and sills the melt must be in contact with the brittle mantle lithosphere. The depth at which this occurs is variable for different rifted margin and is not known for our case. To kinematically reproduce the interpreted magmatic crust, numerically at each time step dt, when an element with mantle phase is becoming a magmatic element according to the rules stated above, we (1) change the phase of this element from dry olivine mantle (Goetze, 1978) to dunite (Shelton, 1981) for volcanic/oceanic crust and (2) we increase its volume by imposing a volumic stress change caused by a strain rate proportional to the accretion of oceanic/volcanic crust at a rate, v_c (m/s) according to:

$$\Delta\sigma_{xx} = -\frac{E\Delta x}{(1-\upsilon^2)v_c dt} \tag{9}$$

and

$$\Delta\sigma_{zz} = \frac{\upsilon\Delta\sigma_{xx}}{(1-\upsilon)} \tag{10}$$

where $\Delta\sigma_{xx}$ and $\Delta\sigma_{zz}$ are the accretionary normal stress change which are to be added to the normal state of stress in each element. E is Young's modulus, υ is Poisson's ratio, Δx is the average width of the elements that are accreting melt and dt the numerical time step.

The resulting deformation corresponds to the accretion of magmatic crust in the element at the rate v_c during the time step dt. When accretion is accommodated by more than one element, the stress change is averaged over the sum of the volume of all magmatic elements. When a column of ocean crust reaches 7 km (average ocean crustal thickness) we assume that it becomes a spreading center and this column takes all accretion to replicate steady state seafloor spreading. This leads to the formation of oceanic crust and the accommodation of most of the extension by magmatic accretion. In addition, at the time of the formation of the spreading we

Table 1
Physical Parameters Used in the Preferred Model

Parameter	Mantle	Serpentinized mantle	Crust	BD crust	Basaltic crust	Sediments	Salt
Density (kg/m^3)	3,300	3,000	2,800	2,800	3,000	2,400–280	2m200
Creep exponent, n	3	3	3	3	3.05	3	3
Creep pre-exponent (MPa^{-n} · s^{-1})	7×10^{4}	1.25×10^{-1}	3×10^{-6}	5×10^{2}	1.25×10^{-1}	3×10^{-6}	3×10^{-6}
Creep Activation Energy (kJ/mol)	520	176	180	300	376	300	300
Friction angle (°)	30-15	5-5	30-15	5-1	30-15	30-15	5-1
Cohesion (MPa)	44-4	4-4	44-4	4-4	44-4	4-4	4-4
Lamé parameters λ, μ (MPa)	3×10^{10}, 3×10^{10}	3×10^{10}, 3×10^{10}	3×10^{10}, 3×10^{10}	3×10^{10}, 3×10^{10}	3×10^{10}, 3×10^{10}	3×10^{10}, 3×10^{10}	3×10^{10}, 3×10^{10}
Energy Threshold (J)	5×10^{7} depth < 6 km, T<400 °C		1×10^{7} depth <15 km, 200<T<350°C				
Thermal Cond (W · m^{-1} · K^{-1})	3.3	3.3	2.8	2.8	3.3	2.2	5

change the temperature of the accreted magmatic crust to 1100 °C to account for the rapid transport of heat by advection at the time of seafloor spreading.

9. Results

When using the exhaustive analysis of the effect of initial thermal and compositional (crustal and mantle rheology) conditions of Svartman Dias et al. (2015), the initial thermal and mechanical boundary conditions imposed in our model lead to the formation of a narrow rift. The corresponding evolution is characterized by the formation of a keystone H-Block and its delamination during hyperextension (Lavier & Manatschal, 2006; Svartman Dias et al., 2015; Van Avendonk et al., 2009). We should expect some differences arising from the development of large offset normal faults and a brittle-ductile shear zone early in the rift evolution. We ran 18 models (Table S1 in the supporting information; models' vtk files and inputs are available on demand) to parameterize the approximate simulation of the interpreted Kwanza-Espirito Santo conjugate margins properly. After running 18 cases, we find that the parameters and conditions associated with model 16 provide the closest match to the interpreted structure and composition of the conjuguate margins (Figures 1 and 2). Here we present this preferred model, by focusing on different aspects of the evolution of the margins in the simulations. We also provide a movie of the material and temperature evolution as supporting information. The parameters used in this simulation are listed in table 1.

9.1. Evolution of the Deformation and Magmatic Accretion

Figures 4 and 5 show the overall development of the conjugate margins. Figure 4 is showing the lithospheric scale evolution, figure 5 is a magnification of the domain around a keystone block bounded by two major normal faults (Keystone H-Block), and of mantle exhumation and seafloor spreading. To facilitate the later model comparison with the interpreted margins' evolution, we write, in parenthesis, after the model time in millions of years, the possible corresponding age interpreted from the observations.

9.1.1. Distributed Stretching Phase

After 5 Myr (140 Ma) of extension (Figure 4a), several normal faults distributed across the width of the model form in response to the extension. The normal faults are rooted in the BDT and initiate the formation of subhorizontal brittle-ductile shear zones.

9.1.2. Necking

At 10 Myr (135 Ma) a subhorizontal brittle-ductile shear zone forms at the crustal BDT and links several normal faults previously rooted at the BDT (Figures 4b and 5a). Two major coupling faults form, initiating the formation of the keystone H-Block. These coupling faults are coupled in the mantle by a localized wide (several km) and steep semibrittle shear zone where a mix of strong brittle feldspar (dark brown) with weak wet quartz (white) form below 350 °C (Figures 4 and 5). The decoupling shear zone initiates at the 350 °C isotherm where semibrittle localization ends up forming a subhorizontal ductile shear zone, by replacing strong brittle feldspar with weak ductile quartz. After 10 Myr of extensional deformation the lithospheric

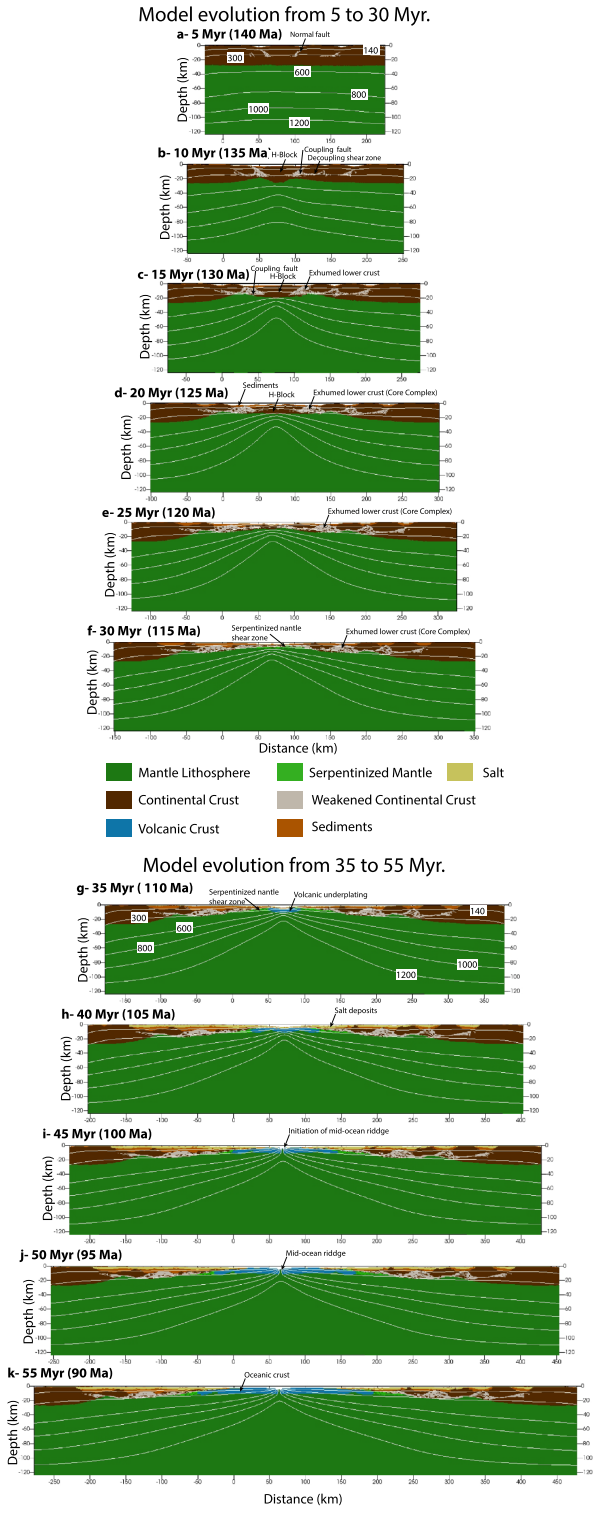

Figure 4. (a to k) Modeled evolution of the margins. The colors correspond to the composition of the lithosphere. Several geotherms are overlaid on top of the composition to follow the thermal evolution as well. The model extends for 550 km forming a 750-km-wide continent to ocean conjugate margin system. See text for details and figure 4 for closed up view of the different phases of evolution. In parenthesis, after the model time in millions of years, we provide the possible corresponding age interpreted from the observations.

keystone couples crustal deformation with deformation in the mantle to form H-Block (Figures 4b and 5a). Meanwhile, lithospheric deformation outside H-Block is still decoupled by decoupling shear zones, and listric normal faults form in the upper crust. We can remark that, at this time, the decoupling subhorizontal shear zone does not extend across H-Block.

Until this point, viscoelastoplastic boudinage of the crust dominates lithospheric deformation. H-Block formation and coupling imposes a deformation wavelength that is dependent on the strength of the mantle and the width of H-Block and is generating a necking instability at the lithosphere asthenosphere boundary (LAB; Chenin et al., 2018). This instability leads to the accelerated thinning of the mantle lithosphere by buoyant upwelling. We observe that the keel of H-Block triggers a significant density contrast with the surrounding mantle (~500 kg/m^3), which results in the enhancement of the upwelling of low viscosity mantle and asthenosphere which rapidly raises the 1000 °C isotherm underneath H-Block. Therefore, in response to coupling and the out-of-balance load generated by the keel of H-Block, depth-dependent thinning (DDT, Huismans and Beaumont (2008)) is triggered and enhanced, as a result of the actively rising asthenosphere. Semibrittle deformation in the middle crust results in the formation of a complex network of a damaged zone in the footwall of the coupling faults and listric normal faults. From 10 Myr (135 Ma) to 15 Myr (130 Ma; Figures 4b and 4c and 5a and 5b) DDT proceeds below H-Block where deformation is coupled, and mid-crustal exhumation is initiated along the coupling faults (Figures 4b and 4c and 5a and 5b). H-Block initially deforms by lower crustal flow in pure shear. This zone of deformation defines the distal basins of the future conjugate margins. Decoupled deformation along the listric normal faults and decoupling shear zones which has occurred outside H-Block defines the proximal basins of the conjugate margins.

9.1.3. Hyperextension

Between 15 Myr (130 Ma) and 25 Myr (120 Ma) most of the extension becomes focused within H-Block (Figures 4c and 4d and 5b and 5c). As the extension evolves and H-Block thins the region becomes hyperextended. Both the exhumation of the lower crust in the footwall of the coupling faults and the formation of normal faults in the center of H-Block occur. The resulting hyperextended domain is thinned to less than 10 km (Figures 4d and 5c) with two characteristic symmetric exhumed core complexes formed entirely of crust exhumed from the middle to lower crust of H-Block. At 25 Myr (120 Ma) normal faults extending in the mantle offset and rotate to form large offset low-angle normal faults that first exhume lower crust (Figures 4d and 4e and 5c and 5d) and then serpentinized mantle below sediments and allochthonous block of upper and lower crust (30 Myr [115 Ma[; Figures 4f and 5e). The crust has thinned and shear zones composed of exhumed serpentinized mantle form on both sides of the remnant of H-Block (Figures 4f and 5e). Both exhumed lower crust and serpentinized mantle behave in a brittle manner at the depth and temperature of the model even though a lot of brittle and ductile damage has occurred in both. The serpentinized mantle is formed below the crustal block (allochthones) and sediments.

9.1.4. Underplating

At 35 Myr (110 Ma; Figures 4g and 5f) magma underplates both the exhumed mantle and the sediments deposited at the seafloor that marks a period between the end of the rift and the beginning of seafloor

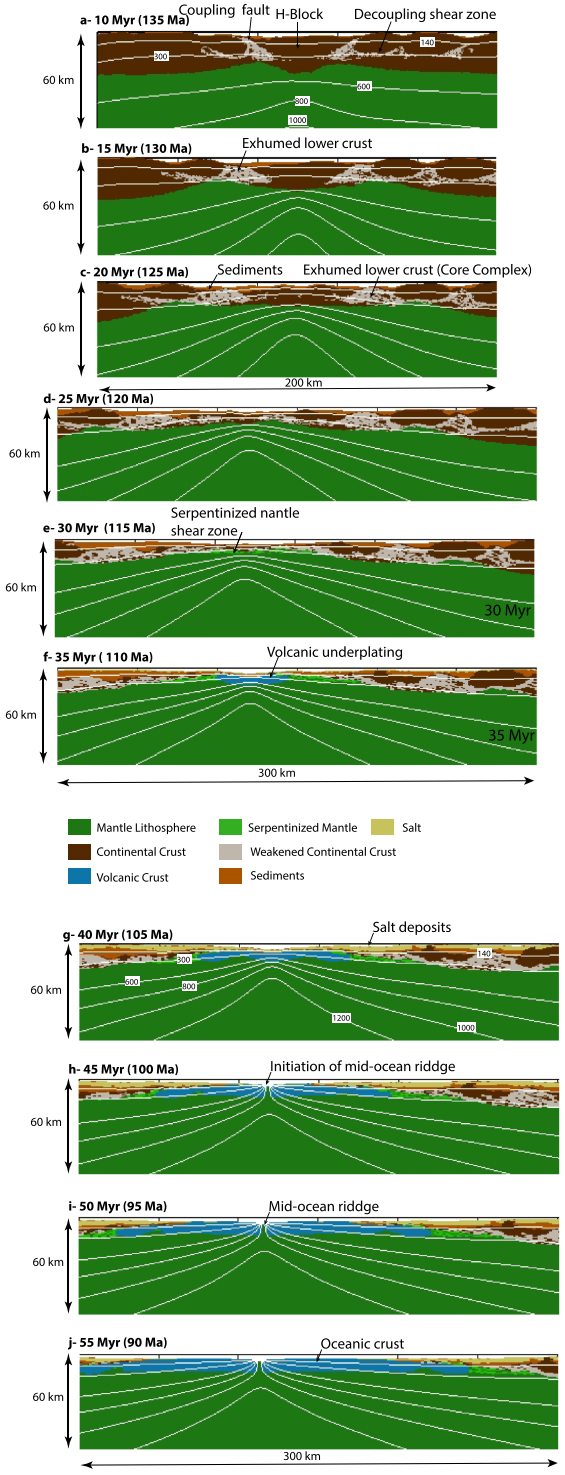

Figure 5. (a to j) Closed up view of the evolution of the modeled margin. 5–10 Myr: Distributed stretching phase. 10–20 Myr: Localized thinning and necking of the lithosphere and DDT. 20–30 Myr: Phase of hyper-extension with exhumation of middle/lower crust and serpentinized mantle. 30–45 Myr: Transitional phase between hyper-extension of the formation of the oceanic crust. 45–55 Myr: Seafloor spreading. See text for details. See legend for composition. In parenthesis, after the model time in millions of years, we provide the possible corresponding age interpreted from the observations.

spreading corresponding to lithospheric breakup. For 10 Myr afterward (40 Myr [105 Ma]; Figures 4h and 5g) magmatic crust is accreted below the hyperextended crust and at the seafloor until it reaches a thickness of 7 km.

9.1.5. Seafloor Spreading

At 45 Myr (100 Ma; Figures 4i and 5h), the model conditions lead to the formation of a spreading center and accretes oceanic crust at a rate of 80% of the full spreading rate occurs, v_c= 0.8 cm/year at the seafloor. For 10 Myr after the initiation of the first complete (7 km thick) column of magmatic material an ocean basin forms by accretion. Accretion continues forming a oceanic crust and a mid-ocean ridge (50 to 55 Myr (95 to 90 Ma); Figures 4j and 4k and 5i and 5j).

9.2. Sedimentation

Two types of sediments are deposited in the basins: (1) siliciclastic sediments below 10 m sea level and (2) salt after 37 Myr (118 Ma) for 1 Myr where sea level is less than 10 m. Since salt is assumed to be deposited between 0 and 10 m sea level, it is forced to occur in the proximal parts of the conjugate margins. This scenario is based on observations made in the South Atlantic margins (Dale et al., 1992; Karner et al., 2003; Wright & Barnett, 2015; Della Porta, 2015; Saller et al., 2016; Tresarus et al. 2017). Siliciclastic sedimentation and erosion due to diffusion modifies the amount of flank uplift along the coupling faults on both sides of H-Block. Sedimentary deposition focuses the heat flow in the sedimentary basins since sediments have lower thermal conductivity than the surrounding crust (Hart et al., 2017). The salt which is modeled with a constant low viscosity of 10^{19} Pa.s which deposits initially in shallow waters flows toward the deepest parts of the basin until about 45 Myr (100 Ma; Figures 4i and 5h). When seafloor spreading initiates and ridge flanks form the salt flows back toward the continent and overlays the underplated basin and the first oceanic crust (Figures 4j and 4k and 5i and 5j).

9.3. Thermal Evolution

The thermal evolution is akin to that observed in previous models including the generation of H-Block (Figures 6a and 6b; Svartman Dias et al., 2015, 2016; Hart et al., 2017). The temperature are also constrained by thermochronological studies (Hart et al., 2017; Smye et al., 2019)

9.3.1. Diffuse stretching phase

An initial period of pure shear dominated stretching (1 to 5 Myr [145 to 140 Ma]; Figure 6a) leads to the initial cooling of the crust as heat flow increases across the margin (McKenzie, 1978).

9.3.2. Necking

When a necking instability initiates and H-Block forms (10 Myr [135 Ma]; Figure 6b), DDT leads to the advection of heat and results in increased heat flux from the mantle lithosphere to the crust (15 to 20 Myr [130 to 125 Ma]; Figures 6b and 6c). The temperature at the base of the crust is >600°*C* (20 Myr [125 Ma]; Figure 6c) as it experiences heating from its initial temperature of 450°*C* (Hart et al., 2017; Smye et al., 2019).

9.3.3. Hyperextension

During the phase of hyperextension (20 to 30 Myr [125 to 115 Ma]; Figures 6d and 6e) cooling initiates and heat advection is balancing diffusion. The crust and mantle are exhumed, and cooling occurs. Temperatures at the distal edge of the basins are greater than 200°*C* producing very high geothermal gradients > 80°*C*/km (Hart et al., 2017).

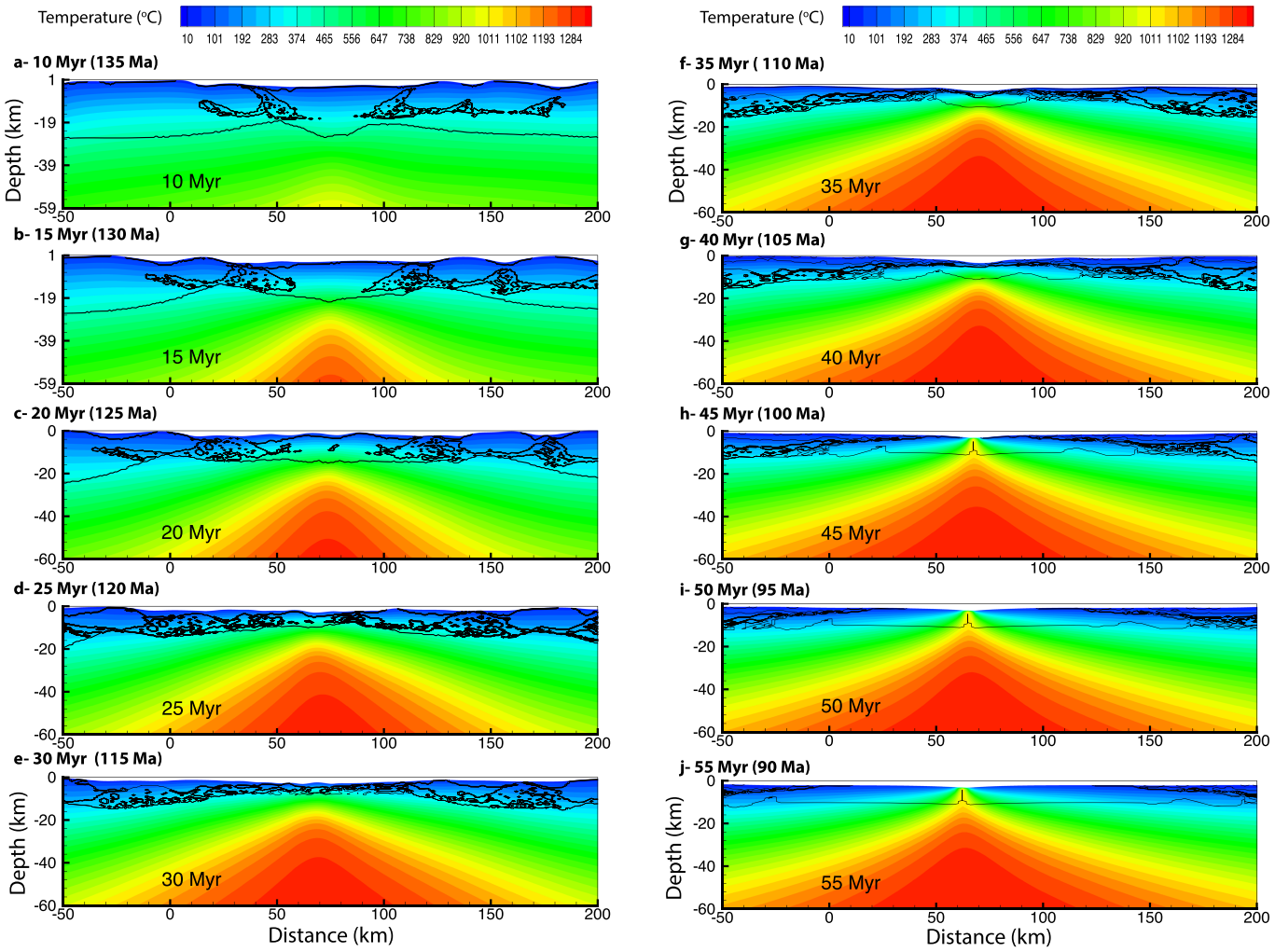

Figure 6. (a to j) Thermal evolution of the modeled margins form necking to seafloor spreading. We distinguished 4 different regimes. (1) Intense DDT from 10 to 20 Myr. (2) Quasi-static thermal state from 25 to 30 Myr. (3) Transition thermal regime while the oceanic crust initiates from 35 to 45 Myr. (4) Seafloor spreading thermal regime from 45 to 55 Myr.

9.3.4. Underplating

During that phase (30 to 40 Myr (115 to 105 Ma; Figures 6f and 6g) the formation of the magmatic crust is initiating reheating until the volcanic crust reaches a thickness of 7 km and a spreading center forms.

9.3.5. Seafloor Spreading

The thermal regime changes as the heat advected by accretion is focused on the spreading center that accumulates 80% of the total extension (Figures 6h to 6j). As spreading follows, the oceanic crust cools away from the axis following a thermal diffusion law.

9.4. Subsidence Evolution

9.4.1. Diffuse Stretching Phase

The first phase of slow subsidence marks the subsidence history for 5 Myr, while the deformation in the crust is decoupled from that in the mantle lithosphere (Figures 7a and 7b).

9.4.2. H-Block Formation

This is followed by a phase of rapid subsidence down to 2,000 below sea level and rift flank uplift up to 1,000 m during the generation of H-Block and the initiation of DDT through lithospheric necking (Huismans & Beaumont, 2008; Chenin et al., 2018; from 5 to 10 Myr [140 to 135 Ma]; Figures 7b and 7c). Individual basins in half-graben structures form on both sides of the central basin floored by the top of H-Block. The basins in the distal parts of the proximal margin are overlying the necking zone and are associated with decoupled

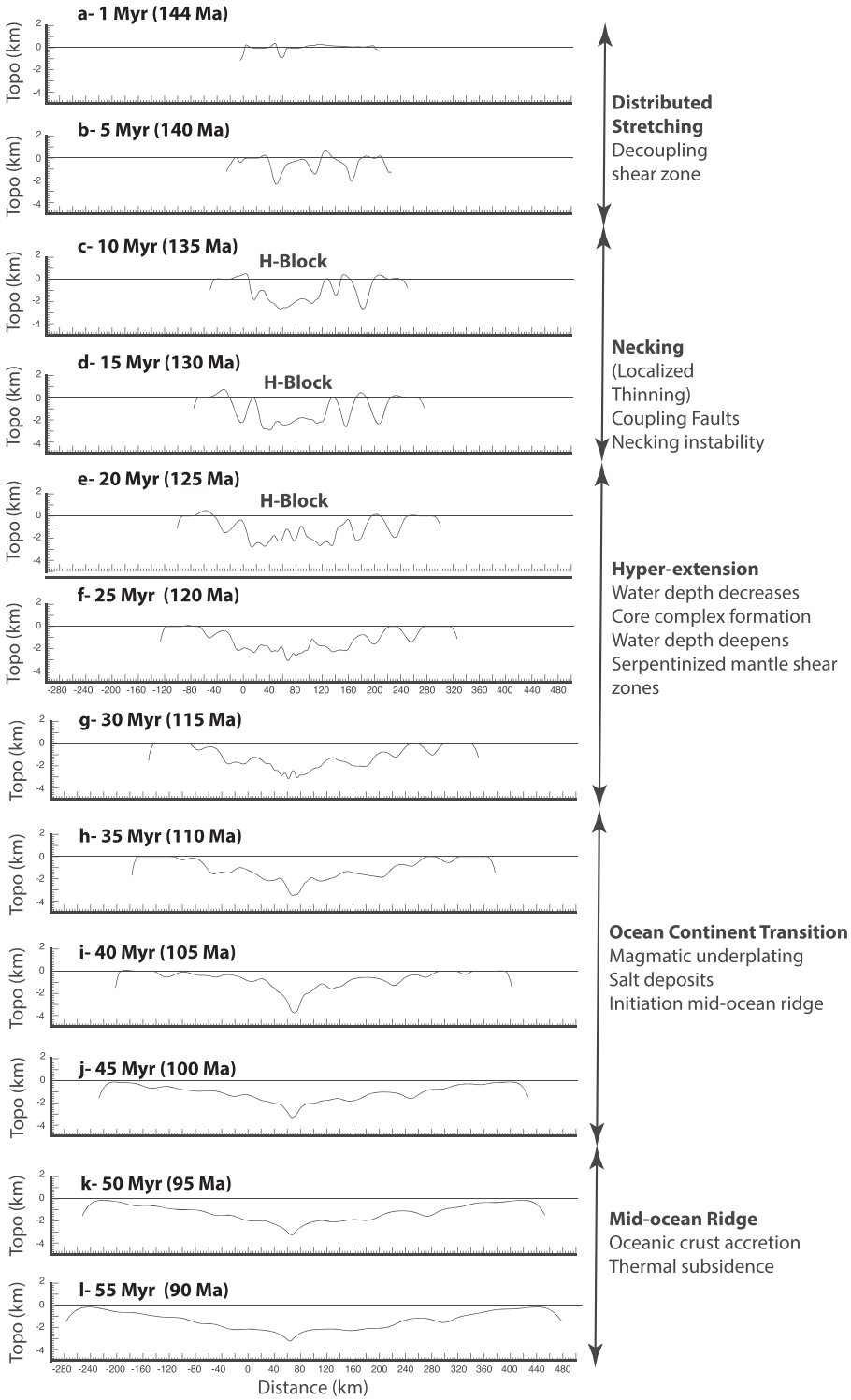

Figure 7. Evolution of the seafloor and ground. (a to f) From 1 to 25 Myr. (g to l) From 30 to 55 Myr. The subsidence shows an initial phase of intense subsidence from 1 to 15 Myr. The area corresponding to the distal margins and H-Block are uplifting from 15 to 25 Myr. When mantle exhumation occurs, the rift axis first subsides (30 to 40 Myr) and then uplifts when the thermal regime changes (45 to 55 Myr) and seafloor spreading is established.

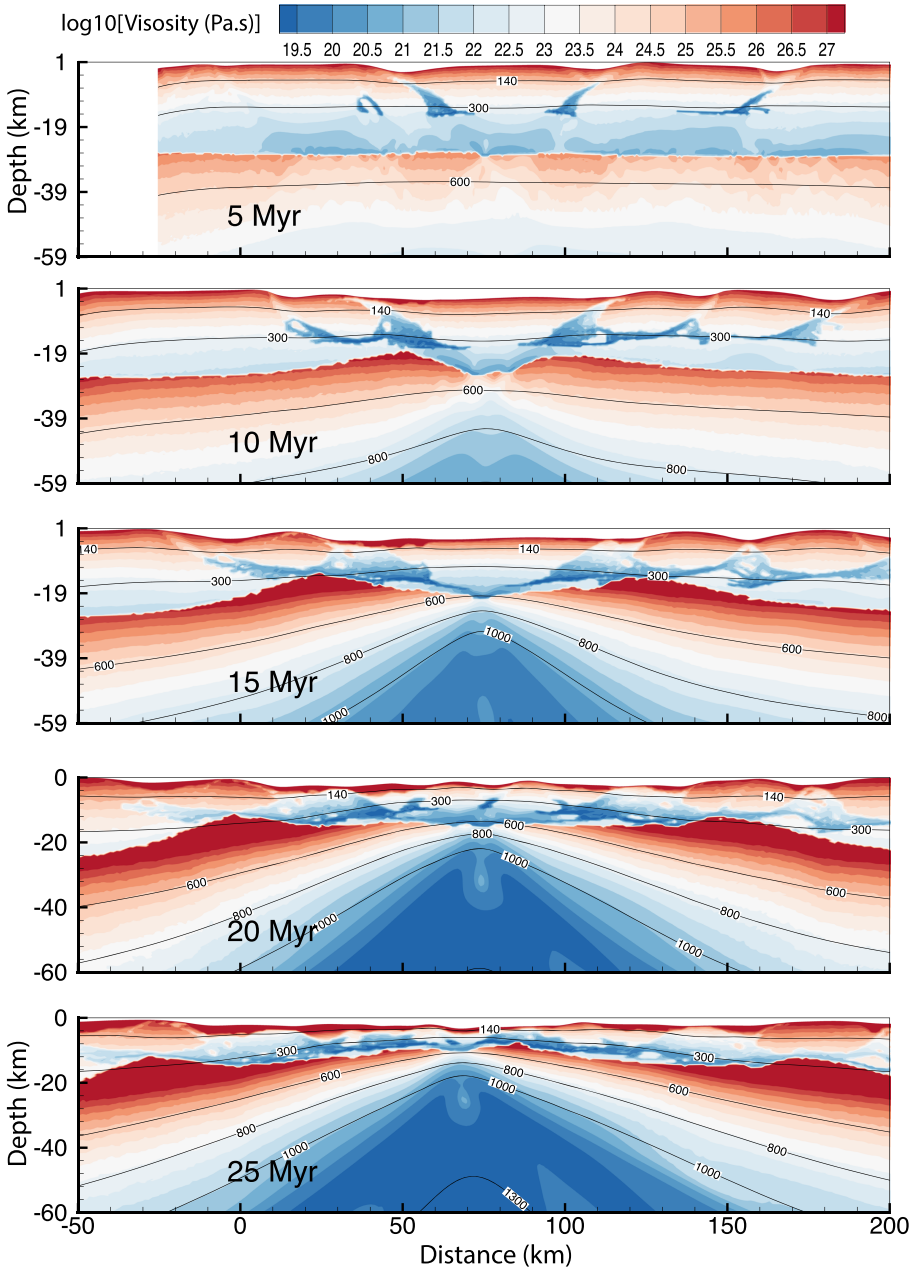

Figure 8. Evolution of the modeled viscosity. With decreasing strength from dark to light red the viscosity displays the brittle zones of the lithosphere. With decreasing viscosity from light to dark blue the viscosity shows the ductile zones in the lithosphere. The dark blue zones in the crust expanding from 5 to 15 Myr correspond to the effect of compositional weakening and the corresponding formation of the large offset normal faults rooted in the decoupling shear zone in the middle to lower crust. Note, that middle and lower crustal material is weakened as it is transported up by the motion along the large offset normal faults. The geotherms are overlain on the computed viscosity field. See text for details.

shear zones. The distal basins are associated with the coupling faults connecting crustal and mantle lithosphere deformation.

9.4.3. Necking

Between 15 and 20 Myr (130 to 125 Ma; Figures 7b and 7c) as DDT reaches its apex the central distal basin is uplifted by 1000 m as several new faults form in this domain and the buoyancy generated by necking of the lithosphere.

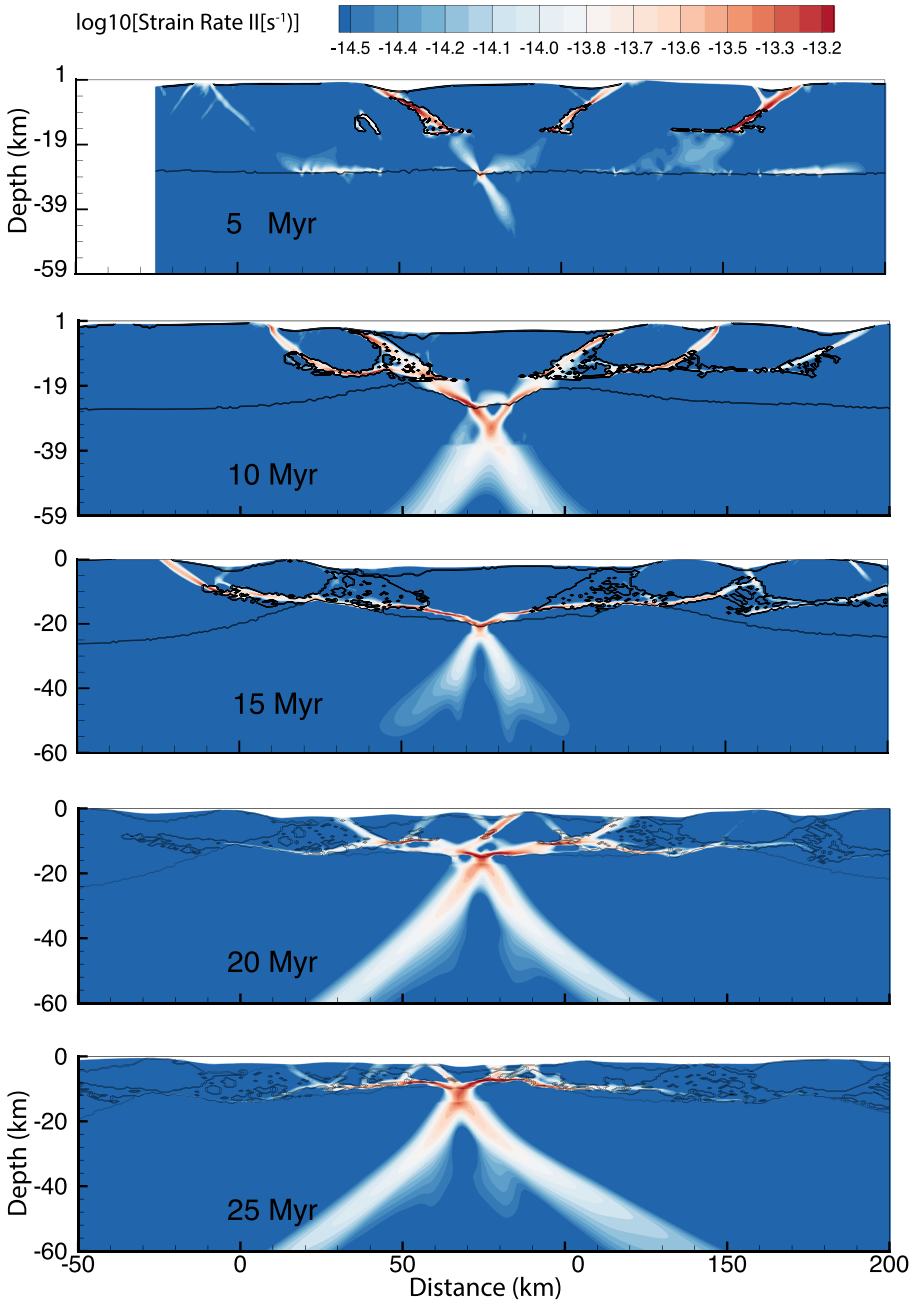

Figure 9. Evolution of the modeled strain rate (square root of the second invariant) displayed for the same times as for the viscosity structure. The compositional distribution is overlapped to show the zones of semibrittle deformation and the potential anastomosing patterns generated by compositional weakening. Remark that even though the weakening is delocalized the instantaneous deformation tends to find a relatively straight path through the semibrittle material. This leads to the formation of very large 100s of km wide zones of decoupling in the middle crust.

9.4.4. Hyperextension

From 20 to 25 Myr (125 to 120 Ma; Figures 7c and 7d) the crust is wholly thinned, and mantle is exhumed along with detachments that are evolving within the serpentinized lithospheric mantle. Due to the extreme crustal thinning in the distal margin, subsidence increases from ~1000 m to ~2500 m below sea level (Figures 7e to 7f).

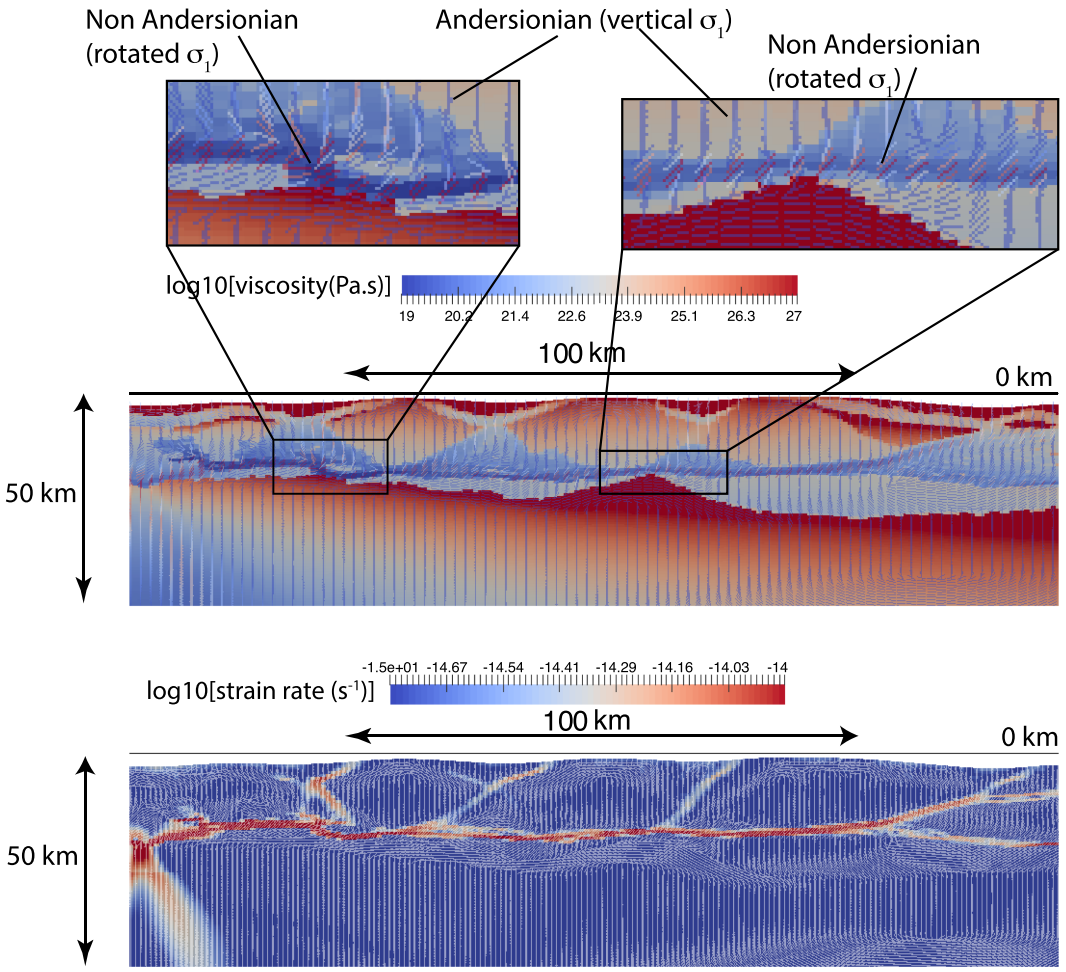

Figure 10. Viscosity and strain rate structure through the large decoupling structures in one of the models. The viscosity shows the formation of a thick zone of semibrittle material in between fault blocks as well as a very localized zone of decoupling in the middle crust (dark blue). The strain rate shows that the deformation is very localized and that slip occurs subhorizontally in the middle crust. Overlain over both the viscosity and strain rate is the orientation of σ_1. While it is vertical and Andersonian in most of the strong upper crustal blocks, its orientation is progressively rotated further away from the vertical in the semibrittle zone and the decoupling shear zone to allow for subhorizontal slip.

9.4.5. Underplating

As magmatic addition replaces crust and sediments in the most distal part of the margin, the margins subsides down to ~4000 m below sea level in 10 Myr (Figure 7f to 7g). Between 35 and 40 Myr, the margins experience a dramatic change in water depth (110 to 105 Ma; Figures 7h and 7i). This event corresponds to the deposition of about 2000 m of salt during 1 Myr at 37 Myr (118 Ma). The salt is first deposited at or above 10 m water depth and flows oceanward in the deeper basins like fluid flowing under the effect of gravity from the area of high (proximal margin) to low (distal margin) topography following a gravity potential. This event brings most of the margin seafloor back between sea level and 1000 m below sea level, including the hyperextended part of the margins, near sea level at 40 Myr (115 Ma; Figure 7i).

9.4.6. Seafloor Spreading

As seafloor spreading is established (100 km away from the edge of the continental margins at 40 Myr [115 Ma]; Figure 7i) the ridge axis and the ridge flank uplift to 3,000 and 2,500 m bsl, respectively (Figure 7j). The margins start then to subside thermally until the mid-oceanic ridge reaches a thermomechanical steady state which corresponds to a balance between the buoyancy of the upwelling asthenosphere and the accretion of new material at the center of the spreading ridge (Figures 7j to 7l).

10. Discussion

The model results provide an approximate self-consistent thermo-mechanical evolution of continental rifting from rift initiation to seafloor spreading. They confirm results from multiple numerical studies on the development of magma-poor margins (Chenin et al., 2018; Huismans & Beaumont, 2008, 2011; Lavier & Manatschal, 2006; Svartman Dias et al., 2015, 2016; Van Avendonk et al., 2009) while extending them to hyperextension, underplating and seafloor spreading. The critical aspects of the results are the formation of extensional features that can be compared to geological structures interpreted from seismic, well, and geophysical data such as: (1) The slip along decoupling shear zones formed through semibrittle processes. (2) In detail, the formation of normal faults rooted in a complex network of basinward, evolving, brittle-ductile shear zones that root in a subhorizontal weak decoupling shear zone (Figures 4 and 5). The resolution of our models does not allow for the development of an anastomosing network of shear zones in the semibrittle crust and serpentinized mantle. However, we believe that our model is analog to such field observations (see Jammes et al., 2015). (3) The uplift and erosion of H-Block as the necking process lead to the active upwelling of the Lithosphere. This can be explained by the transition of the extension from passive to active as the thinning of the mantle lithosphere generates a necking instability at the LAB (Huismans & Beaumont, 2008). (4) The exhumation of core complexes on both sides of H-Block by the exhumation of lower crust along coupling faults as well as the formation of serpentinized mantle shear zone underlying allochthonous crust blocks. The exhumed material is also experiencing semibrittle processes that weaken the footwall of the coupling faults and allow for further slip across the interface of the coupling faults (Lavier et al., 2000).

10.1. Normal Faults and Decoupling Ductile Shear Zone

From distributed stretching to hyperextension, listric normal faults rooted in decoupling brittle-ductile shear zones develop. Figure 8 shows the evolution of the viscosity field, and Figure 9 shows the corresponding square root of the second invariant of strain rate during stretching and hyperextension. The viscosity field allows us to highlight the zones of compositional weakening in the crust, where a weak ductile phase (low viscosity quartz) replaces a strong brittle phase (high viscosity feldspar). The plot of the strain rate (Figure 9) shows the active deformation in the models, precisely how the normal faults, listric normal faults, and the decoupling shear zone accommodate deformation at a given time.

Subhorizontal decoupling shear zones play a critical role in the development of conjugate margins by initially controlling the formation of the proximal basins and later allowing for the establishment of exhumed core complexes on both sides of H-Block during its intense deformation. These shear zones form as a network of subhorizontal fractures that propagate at the depth of the 350°C isotherm (Figures 8 and 9; 5 to 10 Myr [140 to 135 Ma]) following our parameterization (Figure 3). The decoupling zone cannot propagate into H-Block (5 to 10 Myr [140 to 135 Ma]) because deformation there is pure shear dominated and controlled by lower crustal and mantle lithosphere thinning (Figures 8 and 9). Within the footwall of the coupling faults, bounding H-Block, a broad zone of damaged crustal material forms, and evolves into a complex network of shear zones (Figure 9). This material is weaker than the surrounding crust and accommodates the deformation in both pure shear and simple shear mode (Figure 10; 10 and 15 Myr [135 to 130 Ma]). The most prominent damage zones form in the footwall of the initially high-angle coupling faults bounding H-Block (Figure 9; 10 to 15 Myr [135 to 130 Ma]). As extension continues these faults eventually exhume the damaged, middle to lower crust to the seafloor (Figures 5, 8, and 9; 20 Myr) and form core complex like structures (Lavier et al., 1999; Wu et al., 2016). These two core complexes are highly deformed during exhumation, and the ductile shear zones are crosscut by multiple generations of brittle faults (Figure 10). Once the decoupling zone can connect across H-Block (15 Myr [130 Ma]), H-Block dismantlement can proceed until the end of hyperextension (25 Myr [120 Ma]; Figure 9). As a result, a vast decoupling shear zone forms at the base of the crust within the active zone of rifting (Figure 9; 15 to 20 Myr). Some exhumation occurs along the proximal listric normal faults exhuming landward dipping brittle-ductile decoupling shear zones that crosscut brittle detachment faults at high angles (15 to 20 Myr [130 to 125 Ma]).

Listric normal faults rooted in ductile shear zones that decouple the brittle deformation in the upper crust are observed in outcrops associated with the Tethyan margins in the Alps (Bertotti et al., 1993; Mohn et al., 2012). They are also interpreted on many seismic profiles of margins including but not limited to Norway (Osmundsen & Ebbing, 2008), the South China Sea (McIntosh et al., 2014; Savva et al., 2013), and the Iberia margin (Péron-Pinvidic & Manatschal, 2009). The crosscutting relationship between the

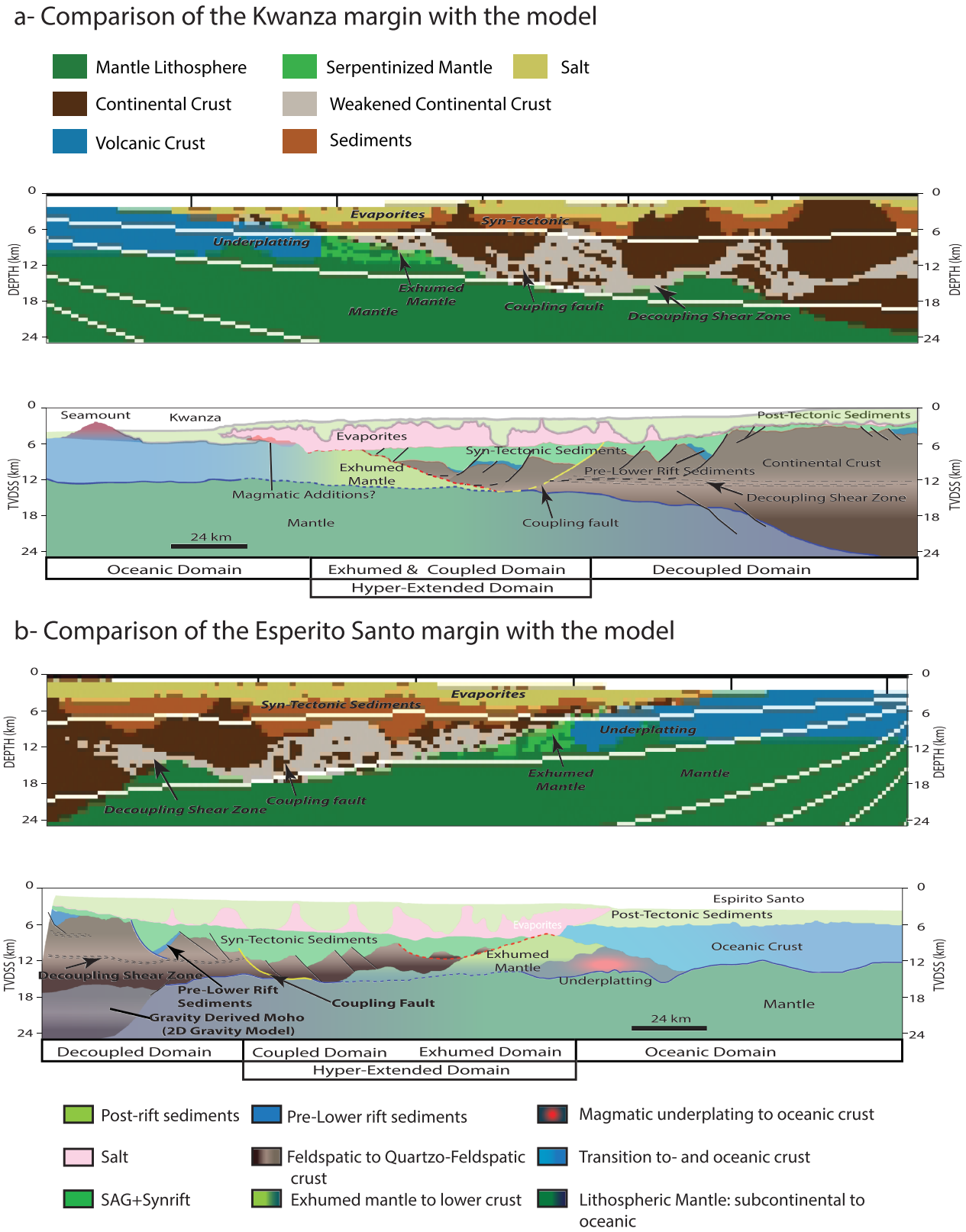

Figure 11. Comparison at the same scale of the interpreted seismic data in Kwanza and Espirito Santo and of the corresponding subdomains in the modeled margins. The legend is added for the numerical models. Remark the similarities while understanding the limitations of both interpretations and numerical models of lithospheric deformation.

landward dipping ductile shear zone and the seaward dipping brittle detachment faults is also observed in the Alps (Mohn et al., 2012) and the Pyrenees (Jammes et al., 2009; Masini et al., 2014). Anastomosing shear zones are also commonly observed in the rift sections in the Alps (Handy & Stünitz, 2002; Manatschal, 2004; Mohn et al., 2012).

10.2. Mechanism for Creep Along Low-Angle Shear Zones and Lower Crustal Removal

Another important aspect of our parameterization is the formation of extensional structures that slip at a shallow dip angle (<30°) and even subhorizontally in the decoupling shear zone. Slip at a low-angle on normal faults has been the subject of numerous debates as it violates the Andersonian theory of faulting that predicts that the lowest dip angle normal fault can slip over is 30° (Buck, 1988). Our parameterization does not violate Andersonian theory faulting as the normal faults move at high-angle in the brittle crust. The dip angle then rotates from high to low in the damaged footwall where the material is brittle-ductile (Figure 9; 10 Myr [135 Ma]). The decoupling shear zone forms as a subhorizontal structure that is subsequently rotated to a higher angle when exhumed in the footwall of the detachments (Figure 8; 20 Myr [125 Ma]). When overlaying the orientation of the maximum principal stress σ_1 on the viscosity structure and the strain rate field of modeled detachment structures (Figure 10), we find that σ_1 is vertical in the upper crust (consistent with Andersonian theory) and rotated by 45° from the vertical in the ductile decoupling shear zone (low viscosity of 10^{19} Pa.s). The rotation of σ_1 in the semibrittle field is consistent with subhorizontal creep that allows for the horizontal motion of the upper crustal block passed the lower crust. The significant strength contrast between the shear zone and the lower crust allows for the lateral removal of the lower crust as a mostly rigid bock even though its strength is lower than that of the brittle upper crust. The removal of the lower crust along subhorizontal ductile shear zones has been documented in detail in the Alps (Eita shear zone; Mohn et al., 2012, Duretz et al., 2016).

10.3. Model Comparison With the Espirito Santo and Kwanza Sections

We plot the final model results at 55 Myr (90 Ma) for both conjugate margins at the same scale as that of the interpreted seismic profiles for the Kwanza and Espirito Santo conjugate margins (Figure 11). We do not provide back-stripped sections for comparison; therefore, it is expected that the modeled crustal and sediment thicknesses are not perfectly matching the interpreted Kwanza and Espirito Santo sections. Many details differ, however, this is to be expected since the numerical models are fully dynamic and their resolution (500 m) is still too low to fit the interpreted structures. Similarly, the water depths are not corresponding either; however, that is not surprising since the model does not simulate 70 Myr of postrift thermal relaxation and sedimentation. The key takeaway from the comparison is that the overall type and scale of structure as well as the sequence of domains from decoupled crust and mantle deformation, to hyperextended (coupled and exhumed mantle), to the formation of a magmatic underplate, and the accretion of oceanic crust are remarkably similar (Figure 11). The model also matches the first-order asymmetric geometries of the necking domains for both interpretations the Angolan Kwanza and Brazilian Espirito-Santos margins (Figures 1 and 2). The model successfully represents the interpreted decoupling shear zone (decoupling domain). Besides, the numerical models suggest that a significant fraction of the hyperextended basement is composed of middle to lower crust that has been exhumed and then faulted by multiple generations of brittle faults, as proposed by Reston and McDermott (2011). We note that the details of the interpreted seismic profiles are not as detailed as the model results. For example, the interpretation of the exhumed middle and lower crust is hard to invoke with the given seismic reflection quality (Figures 1 and 2). The analysis only indicating that is it a hyperextended crust (Figures 1, 2, and 11). As in the interpreted seismic section the transition of the hyperextended domain into a zone of exhumed and serpentinized mantle 30 to 40 km wide. This zone steps up by 5 km over 50 km to the oceanic crust through an area of underplated magmatic bodies in a manner akin to the observations. More model features such as the salt layer flowing over the oceanic crust match the data approximately.

One key aspect of the model to data comparison is the formation of the decoupled and coupled domain interpreted on the seismic sections (Figures 1, 2, and 11). Large offset normal faults rooted in a subhorizontal decoupling shear zone in the middle crust (Figure 11) similar to the Eita shear zone observed in the Alps characterize the decoupled domain. Our modeling exercise suggests that the semibrittle shear zones are the result of the fracture and fluid-driven localization processes at the brittle-ductile transition. The coupled domain is characterized by a coupling fault that extends into the brittle mantle and exhumes highly

deformed lower crust and mantle lithosphere when the temperature conditions allow it (Figures 1, 2, and 11). Coupling occurs after the lower crust has thinned enough that brittle-ductile normal faults can bridge the brittle deformation in the upper crust to that in the brittle upper mantle. Our model suggests that this domain of the margin is, likely to be highly enriched in fluids both meteoric and of mantle origin. Besides, the modeling indicates that all future large offset faults in the decoupling and coupling domains form simultaneously during the stretching phase until the initiation of coupling (0–10 Myr [145–135 Ma]; Figure 10). After that, the decoupling faults are active in the decoupled domain of the margins and rooted over a mega-decoupling shear zone crossing the entire rift (10–15 Myr [135–130 Ma]; Figure 10). This phase is followed by a period of basinward migration of multiple generations of normal faults as hyperextension occurs in H-Block (15–25 Myr [130–120 Ma]; Figure 10). This process suggests a complex synrift sedimentation succession with the oldest sediments being deposited initially across the rift in half grabens. This phase would be followed by the formation of proximal depocenters in listric normal faults. It would eventually end by the basinward migration of the sedimentation with the youngest basins being formed in the distal margin in deepwater settings. This prediction is almost impossible to validate, at present within Angola and Brazil, since very few wells penetrated basement and pre- and synrift sequences in deepwater hyperextended domains. Studies of the Iberian margin suggest that basinward migration of the sedimentation in more and more distal half-grabens is a possible mechanism for the tectonic evolution of hyperextended margins (Ranéro & Pérez-Gussinyé, 2010). Similarly, interpretations from analog Tethyan margins also indicate this diachronous evolution as proposed initially by Masini et al. (2013) and Decarlis et al. (2017).

Two different domains characterize the evolution of the subsidence. In the decoupled domain, the most proximal basins subside early and become inactive after 15 Myr of extension (Figure 7 and 9). In the coupled domain, H-Block first subsides for more than 10 Myr before experiencing uplift until about 20 Myr (125 Ma; Figures 7 and 9). The boundaries of H-Block corresponding the coupling faults first subside and then uplift at or near sea level forming domains favorable to shallow water sediment deposits such as carbonates. As the coupling faults rotate and exhume deeper materials, the width of these shallow-water domains may increase. Expressed in the coupled domain, uplift is generated by DDT and the flexural uplift linked to the sequence of normal faults that accommodate the thinning of H-Block. There the top of the basement is uplifted to 800 m water depth at 20 Myr (Figures 7 and 9). After experiencing a phase of uplift, the center of the basin is subsiding as the mantle is exhumed at 30 Myr (120 Ma). The most dramatic event in the model is that imposed by salt deposition at 37 Myr (118 Ma). Deposit and flow of 2000 m of salt bring large portions of the margin back near sea level and marks a significant environmental change.

The modeled thermal history is broadly consistent with recent thermochronological work that show that DDT is accompanied by an increase in thermal gradient in H-Block and hyperextension by an increase in thermal gradient in the sediments (Beltrando et al., 2015; Hart et al., 2017; Seymour et al., 2016; Smye et al., 2019; Smye & Stockli, 2014). While current seismic images and interpretations in Angola do not resolve the underplated magmatic additions, we do interpret a thickened oceanic crust and also magmatic additions at the OCT. If future modeling could better account for partial melting and melt migration, we may gain further insights into why in some areas magmatic material is added to the base of the crust whereas, in other, volcanics are observed at the surface as flows or seaward dipping reflectors. A higher resolution thermo-mechanical model that could include such processes in 3-D could allow us to extend our understanding of continental rifting to more volcanic settings such as Greenland (Hopper et al., 2003).

11. Conclusions

With the awareness that the seismic interpretations are limited by both the seismic resolution and the lack of well-constraints, and, that model rheological parameterization, initial and boundary conditions are sparsely constrained, we suggest that the following physical processes control the juxtaposition of the critical domains of both the Kwanza and the Espirito Santo sections (Figure 11). (1) The formation of large offset normal faults rooted in a weak decoupling mid-crustal shear zones by compositional weakening. The generation of multiple weak ductile fractures in the brittle crust evolves into a subhorizontal weak layer. Slip at shallow dip angle (<5°) of the mid-crustal decoupling shear zone is allowed by rotation of the principal stresses away from the Andersonian state of stress. (2) When H-Block forms, the initiation of DDT is

triggered by the coupling of the crustal and mantle lithosphere. Continued extension leads to large amounts of DDT during the necking of the lithosphere. (3) Exhumation of both middle/lower crustal and mantle rocks occurs in the hyperextended domain of the conjugate margins and is controlled by the localization of deformation along significant large offset low-angle normal faults bounding H-Block. In the models, this is likely due to the continuous compositional weakening of both crust and mantle lithosphere during extension along large offset normal faults. (4) Large depocenters tend to form sequentially from the proximal to the distal part of the margins. Because of their low thermal conductivity, sediments initially decrease heat flow in the basins. To conserve balance between the high basement heat flow and the low sediment heat flow the thermal gradient in the sedimentary basins must increase. (5) The formation of lower density serpentinized exhumed mantle lithosphere and oceanic crust generates buoyancy and results in a step up in the basement as the transition from the hyperextended to the oceanic domain. (6) Finally, the salt deposited in shallow water in the continental areas flows over the hyperextended and oceanic crust to create a zone where salt overlaps the exhumed mantle and oceanic crust.

While being a first-order approximation, the model parameterization of the semibrittle rheology provides a dynamic picture of the margin that is consistent with the field and seismic interpretations. It demonstrates the critical role that decoupling shear zones play in the evolution of the margin. We propose that since the model is providing a self-consistent structural development of the conjugate margins that the corresponding modeled subsidence and thermal evolution are approaching the behavior of a natural continental rift with little magmatic activity.

Acknowledgments
We thank ConocoPhillips for allowing publication of this work. We thank ION for permission to publish the geoseismic profiles interpreted from the ION seismic data from Angola and Brazil. The results of the numerical models in the form of vtk files, the input files as well as the numerical code used for this study are available on Zenodo (https://zenodo.org/). We also like to thank ConocoPhillips Norge and ConocoPhillips Global New Ventures and Technology departments. This work was supported by a grant from ConocoPhilips Norge to Luc Lavier.

References

Allen, P. A., & Allen, J. R. (2013). *Basin analysis: Principles and application to petroleum play assessment*. 3rd Edition, Cambridge, MA:John Wiley & Sons, pp 642

Aslanian, D., Moulin, M., Olivet, J. L., Unternehr, P., Matias, L., Bache, F., et al. (2009). Brazilian and African passive margins of the Central Segment of the South Atlantic Ocean: Kinematic constraints. *Tectonophysics*, *468*(1-4), 98–112. https://doi.org/10.1016/j.tecto.2008.12.016

Ball, P., Eagles, G., Ebinger, C., McClay, K., & Totterdell, J. (2013). The spatial and temporal evolution of strain during the separation of Australia and Antarctica. *Geochemistry, Geophysics, Geosystems*, *14*, 2771–2799. https://doi.org/10.1002/ggge.20160

Beltrando, M., Manatschal, G., Mohn, G., Dal Piaz, G. V., Brovarone, A. V., & Masini, E. (2014). Recognizing remnants of magma-poor rifted margins in high-pressure orogenic belts: The Alpine case study. *Earth-Science Reviews*, *131*, 88–115. https://doi.org/10.1016/j.earscirev.2014.01.001

Beltrando, M., Stockli, D. F., Decarlis, A., & Manatschal, G. (2015). A crustal-scale view at rift localization along the fossil Adriatic margin of the Alpine Tethys preserved in NW Italy. *Tectonics*, *34*, 1927–1951. https://doi.org/10.1002/2015TC003973

Bertotti, G., Picotti, V., Bernoulli, D., & Castellarin, A. (1993). From rifting to drifting: Tectonic evolution of the South-Alpine upper crust from the Triassic to the Early Cretaceous. *Sedimentary Geology*, *86*(1-2), 53–76. https://doi.org/10.1016/0037-0738(93)90133-P

Blaich, O. A., Faleide, J. I., & Tsikalas, F. (2011). Crustal breakup and continent-ocean transition at South Atlantic conjugate margins. *Journal of Geophysical Research*, *116*, B01402. https://doi.org/10.1029/2010JB007686

Boillot, G., Recq, M., Winterer, E. L., Meyer, A. W., Applegate, J., Baltuck, M., et al. (1987). Tectonic denudation of the upper mantle along passive margins: A model based on drilling results (ODP leg 103, western Galicia margin, Spain). *Tectonophysics*, *132*(4), 335–342. https://doi.org/10.1016/0040-1951(87)90352-0

Brun, J. P., & Beslier, M. O. (1996). Mantle exhumation at passive margins. *Earth and Planetary Science Letters*, *142*(1-2), 161–173. https://doi.org/10.1016/0012-821X(96)00080-5

Brune, S., Heine, C., Clift, P. D., & Pérez-Gussinyé, M. (2017). Rifted margin architecture and crustal rheology: Reviewing Iberia-Newfoundland, Central South Atlantic, and South China Sea. *Marine and Petroleum Geology*, *79*, 257–281. https://doi.org/10.1016/j.marpetgeo.2016.10.018

Brune, S., Heine, C., Pérez-Gussinyé, M., & Sobolev, S. V. (2014). Rift migration explains continental margin asymmetry and crustal hyperextension. *Nature Communications*, *5*(1). https://doi.org/10.1038/ncomms5014

Brune, S., Williams, S. E., Butterworth, N. P., & Müller, R. D. (2016). Abrupt plate accelerations shape rifted continental margins. *Nature*, *536*(7615), 201–204. https://doi.org/10.1038/nature18319

Buck, W. R. (1988). Flexural rotation of normal faults. *Tectonics*, *7*(5), 959–973. https://doi.org/10.1029/TC007i005p00959

Buck, W. R., Lavier, L. L., & Poliakov, A. N. (2005). Modes of faulting at mid-ocean ridges. *Nature*, *434*(7034), 719–723. https://doi.org/10.1038/nature03358

Bürgmann, R., & Dresen, G. (2008). Rheology of the lower crust and upper mantle: Evidence from rock mechanics, geodesy, and field observations. *Annual Review of Earth and Planetary Sciences*, *36*(1), 531–567. https://doi.org/10.1146/annurev.earth.36.031207.124326

Burov, E. B., & Poliakov, A. (2001). Erosion and rheology controls on syn- and post-rift evolution: Verifying old and new ideas using a fully coupled numerical model. *Journal of Geophysical Research*, *106*(B8), 16,461–16,481. https://doi.org/10.1029/2001JB000433

Chenin, P., Schmalholz, S. M., Manatschal, G., & Karner, G. D. (2018). Necking of the lithosphere: A reappraisal of basic concepts with thermo-mechanical numerical modeling. *Journal of Geophysical Research: Solid Earth*, *123*, 5279–5299. https://doi.org/10.1029/2017JB014155

Clark, S. R. (2018). Uncertainty in the breakup, spreading history, and velocity variations of Gondwana. *Gondwana Research*, *53*, 189–196. https://doi.org/10.1016/j.gr.2017.04.029

Contrucci, I., Matias, L., Moulin, M., Géli, L., Klingelhofer, F., Nouzé, H., et al. (2004). Deep structure of the West African continental margin (Congo, Zaïre, Angola), between 5 S and 8 S, from reflection/refraction seismics and gravity data. *Geophysical Journal International*, *158*(2), 529–553. https://doi.org/10.1111/j.1365-246X.2004.02303.x

Cowie, L., Angelo, R. M., Kusznir, N., Manatschal, G., & Horn, B. (2017). Structure of the ocean–continent transition, location of the continent–ocean boundary and magmatic type of the northern Angolan margin from integrated quantitative analysis of deep seismic reflection and gravity anomaly data. *Geological Society, London, Special Publications*, *438*(1), 159–176. https://doi.org/10.1144/SP438.6

Dale, C. T., Lopes, J. R., & Abilio, S. (1992). Takula oil field and the greater Takula area, Cabinda, Angola: Chapter 13.

Davis, G. A., Lister, G. S., & Reynolds, S. J. (1986). Structural evolution of the Whipple and South Mountains shear zones, southwestern United States. *Geology*, *14*(1), 7–10. https://doi.org/10.1130/0091-7613(1986)14<7:SEOTWA>2.0.CO;2

Davis, J. K., & Lavier, L. L. (2017). Influences on the development of volcanic and magma-poor morphologies during passive continental rifting. *Geosphere*, *13*(5), 1524–1540. https://doi.org/10.1130/GES01538.1

Davison, I. (1999). Tectonics and hydrocarbon distribution along the Brazilian South Atlantic margin. *Geological Society, London, Special Publications*, *153*(1), 133–151. https://doi.org/10.1144/GSL.SP.1999.153.01.09

Davison, I. (2007). Geology and tectonics of the South Atlantic Braziliansalt basins. In A. C. Ries, R. W. H. Butler, & R. H. Graham (Eds.). *Deformation of the Continental Crust: The Legacyof Mike Coward* (Vol. 272, pp. 345–359). *Geological Society of London*, Special Publications. Decarlis, A., Beltrando, M., Manatschal, G., Ferrando, S., & Carosi, R. (2017). Architecture of the distal Piedmont-Ligurian rifted margin in NW-Italy: Hints for a flip of the rift system polarity. *Tectonics*, *36*, 2388–2406. https://doi.org/10.1002/2017TC004561

Della Porta, G. (2015). Carbonate build-ups in lacustrine, hydrothermal and fluvial settings: comparing depositional geometry, fabric types and geochemical signature. *Geological Society, London, Special Publications*, *418*(1), 17–68.

Dias, J. L., Sad, A. R. E., Fontana, R. L. & Feijo, F. J. (1994). Bacia de Pelotas. *Boletim Geociencias da Petrobras*, *8*, 235–246.

Driscoll, N. W., & Karner, G. D. (1998). Lower crustal extension across the Northern Carnarvon basin, Australia: Evidence for an eastward dipping detachment. *Journal of Geophysical Research*, *103*(B3), 4975–4991. https://doi.org/10.1029/97JB03295

Duretz, T., Petri, B., Mohn, G., Schmalholz, S. M., Schenker, F. L., & Müntener, O. (2016). The importance of structural softening for the evolution and architecture of passive margins. *Scientific Reports*, *6*(1). https://doi.org/10.1038/srep38704

Duval, B., Cramez, C., & Jackson, M. P. A. (1992). Raft tectonics in the Kwanza basin, Angola. *Marine and Petroleum Geology*, *9*(4), 389–404. https://doi.org/10.1016/0264-8172(92)90050-O

Evain, M., Afilhado, A., Rigoti, C., Loureiro, A., Alves, D., Klingelhoefer, F., et al. & (2015). Deep structure of the Santos Basin-São Paulo Plateau System, SE Brazil, *Journal of Geophysical Research: Solid Earth*, *120*, 5401–5431. https://doi.org/10.1002/2014JB011561

Franke, D. (2013). Rifting, lithosphere breakup and volcanism: Comparison of magma-poor and volcanic rifted margins. *Marine and Petroleum Geology*, *43*, 63–87. https://doi.org/10.1016/j.marpetgeo.2012.11.003

Freudenthal, A. M. (1950). *The inelastic behavior of engineering materials and structures*, (p. 587). New York: Wiley.

Fricke, H. C., Wickham, S. M., & O'Neil, J. R. (1992). Oxygen and hydrogen isotope evidence for meteoric water infiltration during mylonitization and uplift in the Ruby Mountains-East Humboldt Range core complex, Nevada. *Contributions to Mineralogy and Petrology*, *111*(2), 203–221. https://doi.org/10.1007/BF00348952

Gaina, C., Torsvik, T. H., van Hinsbergen, D. J., Medvedev, S., Werner, S. C., & Labails, C. (2013). The African Plate: A history of oceanic crust accretion and subduction since the Jurassic. *Tectonophysics*, *604*, 4–25. https://doi.org/10.1016/j.tecto.2013.05.037

Gallacher, R. J., Keir, D., Harmon, N., Stuart, G., Leroy, S., Hammond, J. O., et al. (2016). The initiation of segmented buoyancy-driven melting during continental breakup. *Nature Communications*, *7*(1), 1–9. https://doi.org/10.1038/ncomms13110

Garfunkel, Z. (1988). Relation between continental rifting and uplifting: Evidence from the Suez rift and northern Red Sea. *Tectonophysics*, *150*(1-2), 33–49. https://doi.org/10.1016/0040-1951(88)90294-6

Goetze, C. (1978). The mechanisms of creep in olivine. *Philosophical Transactions. Royal Society of London*, *288*(1350), 99–119. https://doi.org/10.1098/rsta.1978.0008

Goetze, C., & Evans, B. (1979). Stress and temperature in the bending lithosphere as constrained by experimental rock mechanics. *Geophysical Journal International*, *59*(3), 463–478. https://doi.org/10.1111/j.1365-246X.1979.tb02567.x

Guardado, L. R., Gamboa, L. A. P., & Lucchesi, C. E (1990). Petroleum Geology of the Campos Basin, Brazil: a model for a producing Atlantic-type basin. In J. D. Edwards & P. A. Santogrossi (Eds.), *Divergent~passive margin basins. AAPG Memoir*, 48, 3–79.

Handy, M. R. (1990). The solid-state flow of polymineralic rocks. *Journal of Geophysical Research*, *95*(B6), 8647–8661. https://doi.org/10.1029/JB095iB06p08647

Handy, M. R., & Stünitz, H. (2002). Strain localization by fracturing and reaction weakening—a mechanism for initiating exhumation of subcontinental mantle beneath rifted margins. *Geological Society, London, Special Publications*, *200*(1), 387–407. https://doi.org/10.1144/GSL.SP.2001.200.01.22

Hart, N. R., Stockli, D. F., Lavier, L. L., & Hayman, N. W. (2017). Thermal evolution of a hyper-extended rift basin, Mauléon Basin, western Pyrenees. *Tectonics*, *36*, 1103–1128. https://doi.org/10.1002/2016TC004365

Heine, C., Zoethout, J., & Müller, R. D. (2013). Kinematics of the South Atlantic rift. arXiv preprint arXiv:1301.2096.

Hilairet, N., Reynard, B., Wang, Y., Daniel, I., Merkel, S., Nishiyama, N., & Petitgirard, S. (2007). High-pressure creep of serpentine, interseismic deformation, and initiation of subduction. *Science*, *318*(5858), 1910–1913. https://doi.org/10.1126/science.1148494

Holyoke, C. W. III, & Tullis, J. (2006). Mechanisms of weak phase interconnection and the effects of phase strength contrast on fabric development. *Journal of Structural Geology*, *28*(4), 621–640. https://doi.org/10.1016/j.jsg.2006.01.008

Hopper, J. R., Dahl-Jensen, T., Holbrook, W. S., Larsen, H. C., Lizarralde, D., Korenaga, J., & Kelemen, P. B. (2003). Structure of the SE Greenland margin from seismic reflection and refraction data: Implications for nascent spreading center subsidence and asymmetric crustal accretion during North Atlantic opening. *Journal of Geophysical Research*, *108*(B5), 2269. https://doi.org/10.1029/2002JB001996

Huismans, R., & Beaumont, C. (2011). Depth-dependent extension, two-stage breakup and cratonic underplating at rifted margins. *Nature*, *473*(7345), 74–78. https://doi.org/10.1038/nature09988

Huismans, R. S., & Beaumont, C. (2003). Symmetric and asymmetric lithospheric extension: Relative effects of frictional-plastic and viscous strain softening. *Journal of Geophysical Research*, *108*(B10), 2496. https://doi.org/10.1029/2002JB002026

Huismans, R. S., & Beaumont, C. (2007). Roles of lithospheric strain softening and heterogeneity in determining the geometry of rifts and continental margins. *Geological Society, London, Special Publications*, *282*(1), 111–138. https://doi.org/10.1144/SP282.6

Huismans, R. S., & Beaumont, C. (2008). Complex rifted continental margins explained by dynamical models of depth-dependent lithospheric extension. *Geology*, *36*(2), 163–166. https://doi.org/10.1130/G24231A.1

Huismans, R. S., & Beaumont, C. (2014). Rifted continental margins: The case for depth-dependent extension. *Earth and Planetary Science Letters*, *407*, 148–162. https://doi.org/10.1016/j.epsl.2014.09.032

Jackson, M. P. A., Cramez, C., & Fonck, J.-M. (2000). Role of subaerial volcanic rocks and mantle plumes in creation of South Atlantic margins: Implications for salt tectonics and source rocks. *Marine and Petroleum Geology*, *17*(4), 477–498. https://doi.org/10.1016/S0264-8172(00)00006-4

Jammes, S., & Lavier, L. L. (2016). The effect of bimineralic composition on extensional processes at lithospheric scale. *Geochemistry, Geophysics, Geosystems*, *17*, 3375–3392. https://doi.org/10.1002/2016GC006399

Jammes, S., & Lavier, L. L. (2019). Effect of contrasting strength from inherited crustal fabrics on the development of rifting margins. *Geosphere*, *15*(2), 407–422. https://doi.org/10.1130/GES01686.1

Jammes, S., Lavier, L. L., & Reber, J. E. (2015). Localization and delocalization of deformation in a bimineralic material. *Journal of Geophysical Research: Solid Earth*, *120*, 3649–3663. https://doi.org/10.1002/2015JB011890

Jammes, S., Manatschal, G., Lavier, L., & Masini, E. (2009). Tectonosedimentary evolution related to extreme crustal thinning ahead of a propagating ocean: Example of the western Pyrenees. *Tectonics*, *28*, TC4012. https://doi.org/10.1029/2008TC002406

Jenkyns, H. C. (2018). Transient cooling episodes during Cretaceous Oceanic Anoxic Events with special reference to OAE 1a (Early Aptian). *Philosophical Transactions of the Royal Society A: Mathematical, Physical and Engineering Sciences*, *376*(2130). https://doi.org/10.1098/rsta.2017.0073

Karner, G. D., Driscoll, N. W., & Barker, D. H. N. (2003). Syn-rift regional subsidence across the West African continental margin: The role of lower plate ductile extension. *Geological Society, London, Special Publications*, *207*(1), 105–129. https://doi.org/10.1144/GSL.SP.2003.207.6

Karner, G. D., & Gambôa, L. A. P. (2007). Timing and origin of the South Atlantic pre-salt sag basins and their capping evaporites. *Geological Society, London, Special Publications*, *285*(1), 15–35. https://doi.org/10.1144/SP285.2

Kjøll, H. J., Viola, G., Menegon, L., & Sørensen, B. E. (2015). Brittle-viscous deformation of vein quartz under fluid-rich low greenschist facies conditions. *Journal of Geophysical Research: Solid Earth*, *6*, 681–669. https://doi.org/10.5194/sed-7-213-2015

Kohlstedt, D. L., Evans, B., & Mackwell, S. J. (1995). Strength of the lithosphere: Constraints imposed by laboratory experiments. *Journal of Geophysical Research*, *100*(B9), 17,587–17,602. https://doi.org/10.1029/95JB01460

Korchinski, M., Rey, P. F., Mondy, L., Teyssier, C., & Whitney, D. L. (2018). Numerical investigation of deep-crust behavior under lithospheric extension. *Tectonophysics*, *726*, 137–146. https://doi.org/10.1016/j.tecto.2017.12.029

Kronenberg, A., Segall, P., & Wolf, G. H. (1990). Hydrolytic weakening and penetrative deformation within a natural shear zone. In A. B. Duba, et al. (Eds.), *The Brittle- Ductile Transition in Rocks, Geophysical Monograph Series, 56*, (pp. 21–36). Washington, DC: AGU.

Kröner, A., & Stern, R. J. (2004). Africa: Pan-African orogeny. *Encyclopedia of Geology*, *1*, 1–12.

Kusznir, N. J., Marsden, G., & Egan, S. S. (1991). A flexural-cantilever simple-shear/pure-shear model of continental lithosphere extension: Applications to the Jeanne d'Arc Basin, Grand Banks and Viking Graben, North Sea. *Geological Society, London, Special Publications*, *56*(1), 41–60. https://doi.org/10.1144/GSL.SP.1991.056.01.04

Lavier, L. L., Bennett, R. A., & Duddu, R. (2013). Creep events at the brittle ductile transition. *Geochemistry, Geophysics, Geosystems*, *14*, 3334–3351. https://doi.org/10.1002/ggge.20178

Lavier, L. L., Buck, W. R., & Poliakov, A. N. (1999). Self-consistent rolling-hinge model for the evolution of large-offset low-angle normal faults. *Geology*, *27*(12), 1127–1130. https://doi.org/10.1130/0091-7613(1999)027<1127:SCRHMF>2.3.CO;2

Lavier, L. L., Buck, W. R., & Poliakov, A. N. (2000). Factors controlling normal fault offset in an ideal brittle layer. *Journal of Geophysical Research*, *105*(B10), 23,431–23,442. https://doi.org/10.1029/2000JB900108

Lavier, L. L., & Manatschal, G. (2006). A mechanism to thin the continental lithosphere at magma-poor margins. *Nature*, *440*(7082), 324–328. https://doi.org/10.1038/nature04608

Lemoine, M., Tricart, P., & Boillot, G. (1987). Ultramafic and gabbroic ocean floor of the Ligurian Tethys (Alps, Corsica, Apennines): In search of a genetic model. *Geology*, *15*(7), 622–625. https://doi.org/10.1130/0091-7613(1987)15<622:UAGOFO>2.0.CO;2

Lester, R., Van Avendonk, H. J., McIntosh, K., Lavier, L., Liu, C. S., Wang, T. K., & Wu, F. (2014). Rifting and magmatism in the northeastern South China Sea from wide-angle tomography and seismic reflection imaging. *Journal of Geophysical Research: Solid Earth*, *119*, 2305–2323. https://doi.org/10.1002/2013JB010639

Manatschal, G. (2004). New models for evolution of magma-poor rifted margins based on a review of data and concepts from West Iberia and the Alps. *International Journal of Earth Sciences*, *93*(3), 432–466.

Manatschal, G., & Bernoulli, D. (1999). Architecture and tectonic evolution of nonvolcanic margins: Present-day Galicia and ancient Adria. *Tectonics*, *18*(6), 1099–1119. https://doi.org/10.1029/1999TC900041

Manatschal, G., Froitzheim, N., Rubenach, M., & Turrin, B. D. (2001). The role of detachment faulting in the formation of an ocean-continent transition: Insights from the Iberia Abyssal Plain. *Geological Society, London, Special Publications*, *187*(1), 405–428. https://doi.org/10.1144/GSL.SP.2001.187.01.20

Mancktelow, N. S., & Pennachioni, G. (2005). The control of precursor brittle fracture and fluid–rock interaction on the development of single and paired ductile shear zones. *Journal of Structural Geology*, *27*(4), 645–661. https://doi.org/10.1016/j.jsg.2004.12.001

Marzoli, A., Melluso, L., Morra, V., Renne, P. R., Sgrosso, I., D'antonio, M., et al. (1999). Geochronology and petrology of Cretaceous basaltic magmatism in the Kwanza basin (western Angola), and relationships with the Paraná-Etendeka continental flood basalt province. *Journal of Geodynamics*, *28*(4-5), 341–356. https://doi.org/10.1016/S0264-3707(99)00014-9

Masini, E., Manatschal, G., & Mohn, G. (2013). The alpine Tethys rifted margins: Reconciling old and new ideas to understand the stratigraphic architecture of magma-poor rifted margins. *Sedimentology*, *60*(1), 174–196. https://doi.org/10.1111/sed.12017

Masini, E., Manatschal, G., Mohn, G., & Unternehr, P. (2012). Anatomy and tectono-sedimentary evolution of a rift-related detachment system: The example of the Err detachment (central Alps, SE Switzerland). *Geological Society of America Bulletin*, *124*(9-10), 1535–1551. https://doi.org/10.1130/B30557.1

Masini, E., Manatschal, G., Tugend, J., Mohn, G., & Flament, J. M. (2014). The tectono-sedimentary evolution of a hyper-extended rift basin: The example of the Arzacq–Mauléon rift system (Western Pyrenees, SW France). *International Journal of Earth Sciences*, *103*(6), 1569–1596. https://doi.org/10.1007/s00531-014-1023-8

McIntosh, K., Lavier, L., van Avendonk, H., Lester, R., Eakin, D., & Liu, C. S. (2014). Crustal structure and inferred rifting processes in the northeast South China Sea. *Marine and Petroleum Geology*, *58*, 612–626. https://doi.org/10.1016/j.marpetgeo.2014.03.012

McKenzie, D. (1978). Some remarks on the development of sedimentary basins. *Earth and Planetary Science Letters*, *40*(1), 25–32. https://doi.org/10.1016/0012-821X(78)90071-7

Mohn, G., Karner, G. D., Manatschal, G., & Johnson, C. A. (2015). Structural and stratigraphic evolution of the Iberia–Newfoundland hyper-extended rifted margin: A quantitative modelling approach. *Geological Society, London, Special Publications*, *413*(1), 53–89. https://doi.org/10.1144/SP413.9

Mohn, G., Manatschal, G., Beltrando, M., Masini, E., & Kusznir, N. (2012). Necking of continental crust in magma-poor rifted margins: Evidence from the fossil Alpine Tethys margins. *Tectonics*, *31*, TC1012. https://doi.org/10.1029/2011TC002961

Mohn, G., Manatschal, G., Müntener, O., Beltrando, M., & Masini, E. (2010). Unravelling the interaction between tectonic and sedimentary processes during lithospheric thinning in the Alpine Tethys margins. *International Journal of Earth Sciences*, *99*(S1), 75–101. https://doi.org/10.1007/s00531-010-0566-6

Moulin, M., Aslanian, D., Olivet, J. L., Contrucci, I., Matias, L., Géli, L., et al. (2005). Geological constraints on the evolution of the Angolan margin based on reflection and refraction seismic data (ZaïAngo project). *Geophysical Journal International*, *162*(3), 793–810. https://doi.org/10.1111/j.1365-246X.2005.02668.x

Moulin, M., Aslanian, D., & Unternehr, P. (2010). A new starting point for the South and Equatorial Atlantic Ocean. *Earth-Science Reviews*, *98*(1-2), 1–37. https://doi.org/10.1016/j.earscirev.2009.08.001

Nagel, T. J., & Buck, W. R. (2007). Control of rheological stratification on rifting geometry: A symmetric model resolving the upper plate paradox. *International Journal of Earth Sciences*, *96*(6), 1047–1057. https://doi.org/10.1007/s00531-007-0195-x

Naliboff, J. B., Buiter, S. J. H., Péron-Pinvidic, G., Osmundsen, P. T., & Tetreault, J. (2018). Complex fault interaction controls continental rifting. *Nature Communications*, *8*(1), 1179.

Nirrengarten, M., Manatschal, G., Tugend, J., Kusznir, N. J., & Sauter, D. (2017). Nature and origin of the J-magnetic anomaly offshore Iberia–Newfoundland: Implications for plate reconstructions. *Terra Nova*, *29*(1), 20–28. https://doi.org/10.1111/ter.12240

Oliveira, L. C., Oliveira, R. M. A. G., & Pereira, E. (2018). Seismic characteristics of the onshore Abrolhos magmatism, East-Brazilian continental margin. *Marine and Petroleum Geology*, *89*(2018), 488–499. https://doi.org/10.1016/j.marpetgeo.2017.10.016

Osmundsen, P. T., & Ebbing, J. (2008). Styles of extension offshore mid-Norway and implications for mechanisms of crustal thinning at passive margins. *Tectonics*, *27*, TC6016. https://doi.org/10.1029/2007TC002242

Pérez-Gussinyé, M., & Reston, T. J. (2001). Rheological evolution during extension at nonvolcanic rifted margins: Onset of serpentinization and development of detachments leading to continental breakup. *Journal of Geophysical Research*, *106*(B3), 3961–3975. https://doi.org/10.1029/2000JB900325

Péron-Pinvidic, G., & Manatschal, G. (2009). The final rifting evolution at deep magma-poor passive margins from Iberia-Newfoundland: A new point of view. *International Journal of Earth Sciences*, *98*(7), 1581–1597. https://doi.org/10.1007/s00531-008-0337-9

Péron-Pinvidic, G., Manatschal, G., Masini, E., Sutra, E., Flament, J. M., Haupert, I., & Unternehr, P. (2017). Unravelling the along-strike variability of the Angola–Gabon rifted margin: A mapping approach. *Geological Society, London, Special Publications*, *438*(1), 49–76. https://doi.org/10.1144/SP438.1

Pinto, V. H. G., Manatschal, G., Karpoff, A. M., & Viana, A. (2015). Tracing mantle-reacted fluids in magma-poor rifted margins: The example of Alpine Tethyan rifted margins. *Geochemistry, Geophysics, Geosystems*, *16*, 3271–3308. https://doi.org/10.1002/2015GC005830

Regenauer-Lieb, K., Weinberg, R. F., Rosenbaum, G. (2006). The effect of energy feedbacks on continental strength. *Nature*, *442*, 67–70.

Ranéro, C. R., & Pérez-Gussinyé, M. (2010). Sequential faulting explains the asymmetry and extension discrepancy of conjugate margins. *Nature*, *468*(7321), 294–299. https://doi.org/10.1038/nature09520

Reston, T. (2007). Extension discrepancy at North Atlantic nonvolcanic rifted margins: Depth-dependent stretching or unrecognized faulting? *Geology*, *35*(4), 367–370. https://doi.org/10.1130/G23213A.1

Reston, T. J., & McDermott, K. G. (2011). Successive detachment faults and mantle unroofing at magma-poor rifted margins. *Geology*, *39*(11), 1071–1074. https://doi.org/10.1130/G32428.1

Ros, E., Perez-Gussinye, M., Cavalcanti de Arauj, M., & Morgan, J. P. (2017). Lower Crustal Strength Controls on Melting and Serpentinization at Magma-Poor Margins: Potential Implications for the South Atlantic. *Geochemistry, Geophysics, Geosystems*, *18*, 4538–4557. https://doi.org/10.1002/2017gc007212

Royden, L., & Keen, C. E. (1980). Rifting process and thermal evolution of the continental margin of eastern Canada determined from subsidence curves. *Earth and Planetary Science Letters*, *51*(2), 343–361. https://doi.org/10.1016/0012-821X(80)90216-2

Rybacki, E., Wirth, R., & Dresen, G. (2008). High-strain creep of feldspar rocks: Implications for cavitation and ductile failure in the lower crust. *Geophysical Research Letters*, *35*, L04304. https://doi.org/10.1029/2007GL032478

Rybacki, E., Wirth, R., & Dresen, G. (2010). Superplasticity and ductile fracture of synthetic feldspar deformed to large strain. *Journal of Geophysical Research*, *115*, B08209. https://doi.org/10.1029/2009JB007203

Saller, A., Rushton, S., Buambua, L., Inman, K., McNeil, R., & Dickson, J. T. (2016). Presalt stratigraphy and depositional systems in the Kwanza Basin, offshore Angola. *AAPG Bulletin*, *100*(07), 1135–1164. https://doi.org/10.1306/02111615216

Savva, D., Meresse, F., Pubellier, M., Chamot-Rooke, N., Lavier, L., Po, K. W., & Lamy, G. (2013). Seismic evidence of hyper-stretched crust and mantle exhumation offshore Vietnam. *Tectonophysics*, *608*, 72–83. https://doi.org/10.1016/j.tecto.2013.07.010

Sayers, J., Symonds, P. A., Direen, N. G., & Bernardel, G. (2001). Nature of the continent-ocean transition on the non-volcanic rifted margin of the central Great Australian Bight. *Geological Society, London, Special Publications*, *187*(1), 51–76. https://doi.org/10.1144/GSL.SP.2001.187.01.04

Schmitt, R. D. S., Trouw, R., Van Schmus, W. R., Armstrong, R., & Stanton, N. S. G. (2016). The tectonic significance of the Cabo Frio Tectonic Domain in the SE Brazilian margin: A Paleoproterozoic through Cretaceous saga of a reworked continental margin. *Brazilian Journal of Geology*, *46*(suppl 1), 37–66. https://doi.org/10.1590/2317-4889201620150025

Scholz, C. H. (2002). *The mechanics of earthquakes and faulting*, (p. 471). Cambridge: Cambridge University Press.

Seymour, N. M., Stockli, D. F., Beltrando, M., & Smye, A. J. (2016). Tracing the thermal evolution of the Corsican lower crust during Tethyan rifting. *Tectonics*, *35*, 2439–2466. https://doi.org/10.1002/2016TC004178

Shelton, G. (1981). Experimental flow laws for crustal rocks. *EOS. Transactions of the American Geophysical Union*, *62*, 396.

Sibson, R. H. (1977). Fault rocks and fault mechanisms. *Journal of the Geological Society*, *133*(3), 191–213. https://doi.org/10.1144/gsjgs.133.3.0191

Smye, A., Lavier, L. L., Zack, T., & Stockli, D. F. (2019). Episodic heating of continental lower crust during extension: A thermal modeling investigation of the Ivrea-Verbano Zone. *Earth and Planetary Science Letters*, *521*, 158–168, ISSN 0012-821X. https://doi.org/10.1016/j.epsl.2019.06.015

Smye, A. J., & Stockli, D. F. (2014). Rutile U–Pb age depth profiling: A continuous record of lithospheric thermal evolution. *Earth and Planetary Science Letters*, *408*, 171–182.

Stewart, K., Turner, S., Kelley, S., Hawkesworth, C., Kirstein, L., & Mantovani, M. (1996). 3-D, ^{40}Ar–^{39}Ar geochronology in the Parana continental flood basalt province. *Earth and Planetary Science Letters*, *143*(1-4), 95–109. https://doi.org/10.1016/0012-821X(96)00132-X

Stipp, M., Stünitz, H., Heilbronner, R., & Schmid, S. M. (2002). The eastern Tonale fault zone: A "natural laboratory" for crystal plastic deformation of quartz over a temperature range from 250 to 700 °C. *Journal of Structural Geology*, *24*(12), 1861–1884. https://doi.org/10.1016/S0191-8141(02)00035-4

Sutra, E., Manatschal, G., Mohn, G., & Unternehr, P. (2013). Quantification and restoration of extensional deformation along the Western Iberia and Newfoundland rifted margins. *Geochemistry, Geophysics, Geosystems*, *14*, 2575–2597. https://doi.org/10.1002/ggge.20135

Svartman Dias, A. E., Hayman, N. W., & Lavier, L. L. (2016). Thinning factor distributions viewed through numerical models of continental extension. *Tectonics*, *35*, 3050–3069. https://doi.org/10.1002/2016TC004266

Svartman Dias, A. E., Lavier, L. L., & Hayman, N. W. (2015). Conjugate rifted margins width and asymmetry: The interplay between lithospheric strength and thermomechanical processes. *Journal of Geophysical Research: Solid Earth*, *120*, 8672–8700. https://doi.org/10.1002/2015JB012074

Tan, E., Lavier, L. L., Van Avendonk, H. J., & Heuret, A. (2012). The role of frictional strength on plate coupling at the subduction interface. *Geochemistry, Geophysics, Geosystems*, *13*, Q10006. https://doi.org/10.1029/2012GC004214

Tedeschi, L. R., Jenkyns, H. C., Robinson, S. A., Sanjinés, A. E. S., Viviers, M. C., Quintaes, C. M. S. P., & Vazquez, J. C. (2017). New age constraints on Aptian evaporites and carbonates from the South Atlantic: Implications for Oceanic Anoxic Event 1a. *Geology*, *45*, 543–546. https://doi.org/10.1130/G38886.1

Torsvik, T. H., Rousse, S., Labails, C., & Smethurst, M. A. (2009). A new scheme for the opening of the South Atlantic Ocean and the dissection of an Aptian salt basin. *Geophysical Journal International*, *177*(3), 1315–1333. https://doi.org/10.1111/j.1365-246X.2009.04137.x

Trouw, R., Heilbron, M., Ribeiro, A., Paciullo, F., Valeriano, C. M., Almeida, H., et al. (2000). The central segment of the Ribeira belt. In U. G. Cordani, E. J. Milani, A. Thomaz-Filho, & D. A. Campos (Eds.), *Tectonic Evolution of South America*, (pp. 287–310). Rio de Janeiro, Brazil: 31st International Geological Congress.

Tugend, J., Gillard, M., Manatschal, G., Nirrengarten, M., Harkin, C., Epin, M.-E., et al. (2018). Reappraisal of the magma-rich versus magma-poor rifted margin archetypes. *Geological Society, London, Special Publications*, *476*. https://doi.org/10.1144/SP476.9

Tugend, J., Manatschal, G., Kusznir, N. J., & Masini, E. (2015). Characterizing and identifying structural domains at rifted continental margins: Application to the Bay of Biscay margins and its Western Pyrenean fossil remnants. In G. M. Gibson, F. Roure, & G. Manatschal (Eds.), *Sedimentary basins and crustal processes at continental margins: From modern hyper-extended margins to deformed ancient analogues*, *Special Publications*, (Vol. 413, pp. 171–203). London: Geological Society. https://doi.org/10.1144/SP413.3

Tugend, J., Manatschal, G., Kusznir, N. J., Masini, E., Mohn, G., & Thinon, I. (2014). Formation and deformation of hyper-extended rift systems: Insights from rift domain mapping in the Bay of Biscay-Pyrenees. *Tectonics*, *33*, 1239–1276. https://doi.org/10.1002/2014TC003529

Unternehr, P., Péron-Pinvidic, G., Manatschal, G., & Sutra, E. (2010). Hyper-extended crust in the South Atlantic: In search of a model. *Petroleum Geoscience*, *16*(3), 207–215. https://doi.org/10.1144/1354-079309-904

Van Avendonk, H. J., Lavier, L. L., Shillington, D. J., & Manatschal, G. (2009). Extension of continental crust at the margin of the eastern Grand Banks, Newfoundland. *Tectonophysics*, *468*(1-4), 131–148. https://doi.org/10.1016/j.tecto.2008.05.030

Watts, A. B. (2002). *Isostasy and Flexure of the Lithosphere*, (p. 458). Cambridge: Cambridge University Press.

Weinberg, R. F., Regenauer-Lieb, K., & Rosenbaum, G. (2007). Mantle detachment faults and the breakup of cold continental lithosphere. *Geology*, *35*(11), 1035–1038. https://doi.org/10.1130/G23918A.1

Whitmarsh, R. B., Manatschal, G., & Minshull, T. A. (2001). Evolution of magma-poor continental margins from rifting to seafloor spreading. *Nature*, *413*(6852), 150–154. https://doi.org/10.1038/35093085

Wintsch, D. J., Christoffersen, R., & Kronenberg, A. K. (1995). Fluid-rock reaction weakening of fault zones. *Journal of Geophysical Research*, *100*(B7), 13,021–13,032. https://doi.org/10.1029/94JB02622

Wright, V. P., & Barnett, A. J. (2015). An abiotic model for the development of textures in some South Atlantic early Cretaceous lacustrine carbonates. *Geological Society, London, Special Publications*, *418*(1), 209–219. https://doi.org/10.1144/SP418.3

Wu, G., & Lavier, L. L. (2016). The effects of lower crustal strength and preexisting midcrustal shear zones on the formation of continental core complexes and low-angle normal faults. *Tectonics*, *35*, 2195–2214. https://doi.org/10.1002/2016TC004245